

Supplementary Information

Amide-functional lanthanide metal-organic frameworks: smart double ratiometric fluorescent sensing of thiodiglycolic acid and tunable luminescence

Xu Zhang,^a Jiahui Yu,^a Xin Li,^a Chengqi Jiao,^{*a, b} Yanyu Zhu,^{*a} Hanwen Zheng,^a Zhengang Sun^{*a}

^aSchool of Chemistry and Chemical Engineering, Liaoning Normal University, Dalian 116029, P. R. China

^bState Key Laboratory of Fine Chemicals, Dalian University of Technology, Dalian 116024, P. R. China.

*Corresponding authors.

E-mail: jiaochengqi1989@163.com; summeryzhu@163.com; szg188@163.com.

Contents:

Experimental section.....	5
Fig. S1. IR spectra of Ln-DMF (a) and Ln-DMA (b).....	8
Fig. S2. Coordination modes of the H ₃ L ligand in Tb-DMF (a) and Tb-DMA (b).....	8
Fig. S3. PXRD patterns of Ln-DMF (a) and Ln-DMA (b).....	9
Fig. S4. PXRD patterns of Eu_xTb_{1-x}-DMA and Gd_{0.95}Tb_{0.02}Eu_{0.03}-DMA	9
Fig. S5. PXRD patterns of Tb-DMF (a) and Tb-DMA (b) soaked in boiling water for 4 h and soaked in water for 24 h and exposed to air for 60 d.....	10
Fig. S6. PXRD patterns of Tb-DMF (a) and Tb-DMA (b) soaked in water solution with different pH for 10 h.....	10
Fig. S7. FT-IR spectra of Tb-DMF (a) and Tb-DMA (b) soaked in water solution with different pH for 10 h.....	11
Fig. S8. TG curves of Ln-DMF (a) and Ln-DMA (b).....	11
Fig. S9. PXRD patterns of Tb-DMF (a) and Tb-DMA (b) under different temperatures.....	12
Fig. S10. Solid-state luminescent spectra of H ₃ L.....	12
Fig. S11. CIE chromaticity diagrams of Ln-DMF (a) and Ln-DMA (b).....	13
Fig. S12. Solid-state fluorescence decay curves of Eu-DMF (a) and Tb-DMF (b).....	13
Fig. S13. Solid-state fluorescence decay curves of Eu-DMA (a) and Tb-DMA (b).....	14
Fig. S14. Solid-state fluorescence decay curves of Gd-DMF (a) and Gd-DMA (b).....	14
Fig. S15. (a) UV-Vis absorption spectrum of H ₃ L; (b) Diagram of energy transfer process in Ln-DMF and Ln-DMA	15
Fig. S16. The emission spectra of Tb-DMF , Tb-DMF+TDGA (a) and Tb-DMA , Tb-DMA+TDGA (b).....	15
Fig. S17. Time-dependent luminescence intensity ratios (I_{421}/I_{550} , I_{417}/I_{550}) for Tb-DMF (a) and Tb-DMA (b) in water solution.....	16

Fig. S18. CIE chromaticity diagram showing the variations of fluorescent color coordinates of Tb-DMF (a) and Tb-DMA (b) dispersions in different TDGA concentrations.....	16
Fig. S19. Luminescent spectra of Tb-DMF (a) and Tb-DMA (b) after the addition of TDGA at different times.....	17
Fig. S20. Luminescent spectra of Tb-DMF (a) and Tb-DMA (b) suspensions with various urine components.....	17
Fig. S21. PXRD patterns of Tb-DMF (a) and Tb-DMA (b) before and after detection of TDGA.....	18
Fig. S22. FT-IR spectra of Tb-DMF (a) and Tb-DMA (b) before and after detection of TDGA.....	18
Fig. S23. The full XPS spectra and O1s XPS of Tb-DMF (a, c) and Tb-DMA (b, d).....	19
Fig. S24. (a, c) N ₂ adsorption and desorption isotherms at 77 K of the Tb-DMF/Tb-DMA samples before and after sensing TDGA; (b, d) Pore size distribution curves of Tb-DMF/Tb-DMA samples before and after sensing TDGA based on N ₂ adsorption isotherms at 77 K....	19
Fig. S25. Emission decay profiles of Tb-DMF (a) and Tb-DMA (b) suspensions before and after detection of TDGA.....	20
Fig. S26. UV–Vis absorption spectra of TDGA, Tb-DMF (a) and Tb-DMA (b) in aqueous solutions.....	20
Fig. S27. HOMO and LUMO energy levels of the TDGA and the H ₃ L ligand calculated by density functional theory (DFT) at B3LYP/6–31G (d, p) basis set.....	21
Fig. S28. TG curves of Ln-DMA and Tb_{0.5}Eu_{0.5}-DMA	21
Fig. S29. FT-IR spectra of Eu _x Tb _{1-x} -DMA and Gd _{0.95} Tb _{0.02} Eu _{0.03} -DMA.....	22
Fig. S30. Emission decay profiles of Eu _x Tb _{1-x} -DMA.....	22
Fig. S31. Luminescent emission spectra of Eu-DMA (a), Eu_{0.8}Tb_{0.2}-DMA (b), Eu_{0.6}Tb_{0.4}-DMA (c), Eu_{0.4}Tb_{0.6}-DMA (d), Eu_{0.2}Tb_{0.8}-DMA (e), and Tb-DMA (f) under different excitation wavelengths.....	23

Fig. S32. CIE chromaticity diagrams showing the variation of fluorescent color coordinates of Eu-DMA (a), Eu_{0.8}Tb_{0.2}-DMA (b), Eu_{0.6}Tb_{0.4}-DMA (c), Eu_{0.4}Tb_{0.6}-DMA (d), Eu_{0.2}Tb_{0.8}-DMA (e), and Tb-DMA (f) under different excitation wavelengths.....	23
Fig.S33. (a) Photographs of flower using different colors of Eu_xTb_{1-x}-DMA@PMMA composites under daylight, 302 nm and 365 nm UV lamp; (b) Luminescent emission spectrum (inset, photographs of powder and aqueous solution of Gd_{0.95}Tb_{0.02}Eu_{0.03}-DMA ; (c) CIE chromaticity diagram of Gd_{0.95}Eu_{0.03}Tb_{0.02}-DMA under 365 nm UV light (inset, image of Gd_{0.95}Eu_{0.03}Tb_{0.02}-DMA led device).....	24
Table S1. Crystal data and structure refinements for Ln-DMF	25
Table S2. Selected bond lengths (Å) and angles (°) for Tb-DMF	26
Table S3. Crystal data and structure refinements for Ln-DMA	27
Table S4. Selected bond lengths (Å) and angles (°) for Tb-DMA	28
Table S5. Comparison of the proposed sensor for TDGA detection with other methods.....	28
Table S6. Determination of TDGA with Tb-DMF in simulated urine samples by standard addition method.....	28
Table S7. Determination of TDGA with Tb-DMA in simulated urine samples by standard addition method.....	29
Table S8. Determination of TDGA with Tb-DMF in real urine samples by standard addition method.....	29
Table S9. Determination of TDGA with Tb-DMA in real urine samples by standard addition method.....	29
Table S10. Smartphone-based fluorescent detection of TDGA in real samples.....	30
Table S11. Colour coordinates of Ln-DMA , Eu_xTb_{1-x}-DMA and Gd_{0.95}Tb_{0.02}Eu_{0.03}-DMA according to CIE 1931 with varied quantum yields and lifetimes.....	31
Table S12. Summary of the quantum yields of the reported white-light-emission doped MOFs.....	31
Table S13. Selected bond lengths (Å) and angles (°) for Eu-DMF	32
Table S14. Selected bond lengths (Å) and angles (°) for Gd-DMF	33

Table S15. Selected bond lengths (Å) and angles (°) for **Gd-DMA**34

Table S16. Selected bond lengths (Å) and angles (°) for **Gd-DMA**.....35

1. Experimental section

1.1 Materials and measurements

All reagents and solvents were purchased from commercial suppliers and utilized without further purification. The H₃L ligand was prepared according to the literature reported previously.¹ Elemental analyses (C, H and N) were performed on a PE-2400 elemental analyzer. IR spectra were measured using a Bruker AXS TENSOR-27 FT-IR spectrometer from 4000 to 400 cm⁻¹. Thermogravimetric analyses (TG) were performed using a PerkinElmer Pyris Diamond TG-DTA thermal analyses system in the range of 50–1100 °C with a heating rate of 10 °C min⁻¹. Powder X-ray diffraction (PXRD) pattern was conducted on a Bruker AXS D8 ADVANCE diffractometer with Cu K α radiation. UV-Vis spectra were measured on a Lambda 35 spectrophotometer. Luminescent spectra were measured using a HITACHI F-7000 spectrofluorimeter. XPS was performed using a K-Alpha Xray photoelectron spectrometer. Luminescent lifetime was recorded on a HORIBA Scientific FluoroMax-4 TCSPC spectrofluorometer. The highest occupied molecular orbital (HOMO) and the lowest unoccupied molecular orbital (LUMO) energy levels of H₃L ligand and TDGA were calculated by the density functional theory (DFT) method at the B3LYP/6-31G*(d) level in the Gaussian 09 program package.² The non-covalent interaction (NCI) diagrams were analysis by Multiwfn-3.7 and VMD.^{3,4}

1.2 Crystallographic studies

Data collections for **Ln-DMF** and **Ln-DMA** were achieved on a Bruker AXS Smart APEX II CCD X-diffractometer with graphite-monochromated Mo K α ($\lambda = 0.71073 \text{ \AA}$) at 296(2) K. The Olex 2 program was used to solve the structures by direct methods and refined on F^2 by full-matrix least-squares methods.⁵ All non-H atoms were refined with anisotropic thermal parameters. A summary of the crystallographic data and refinement parameters are listed in Table S1 and S2. Bond distances and angles of **Ln-DMF** and **Ln-DMA** are provided in Table S3–S8.

1.3 Luminescent measurement

The detection procedure was performed as follows: 1.0×10^{-2} M of TDGA solutions with various volumes were added into the **Tb-DMF** and **Tb-DMA** suspensions (2.0 mg **Tb-DMF/Tb-DMA** in 2.0 mL deionized water after treating by ultrasonication for 15 min), respectively. The emission spectra were recorded. Each data was performed three times. To explore the selectivity and anti-interference abilities, 2.0 mg of **Tb-DMF/Tb-DMA** powder was immersed into the 3.0 mL aqueous solution (1.0×10^{-3} M), including different urine chemicals of NaCl, KCl, NH₄Cl, Na₂SO₄, Urea, Glucose, Creatine, Creatinine in the absence or presence of TDGA, followed by ultrasonication for approximately 15 min, and then obtained the stable suspensions. After that, fluorescence spectra were collected. To explore the actual application of the proposed double ratiometric fluorescent probe, the simulated urine sample without TDGA was selected as a case, and spiked with TDGA (1.0×10^{-2} M) possessing different concentrations. In addition, the TDGA sensing in diluted human urine samples was also conducted. Fresh human urine sample was collected from a healthy volunteer. Firstly, the initial urine sample was filtrated by filter membrane (0.22 μ m) and diluted 1000 fold. Then the diluted urine was spiked with TDGA possessing different concentrations for the sensing experiment.

1.4 Smartphone-assisted on-site detection of TDGA

A simple, concise, and portable method was designed for ultrafast and on-site detection of analytes. This system utilized a 365 nm LED UV lamp as an excitation light source attached to a lamp holder for the **Tb-DMF/Tb-DMA** excitation. Samples were positioned directly under UV light to minimize light distortion caused by distance. The smartphone then analyzed the signals by measuring the RGB values using a color-picker app. A black box was also used to integrate the above-mentioned components, enabling real-time TDGA testing.

1.5 Methods for preparing anti-counterfeiting film

The polymer of PMMA (1.0 g), DMF (6 mL), and **Eu_xTb_{1-x}-DMA** (0.30 mg) were mixed and stirred at room temperature for 8 h. Then, the mixed solution was dropped onto a quartz wafer ($5.0 \times 10.0 \text{ cm}^2$), which was annealed at room temperature for 12 h. Finally, a **PMMA@Eu_xTb_{1-x}-DMA** was obtained.

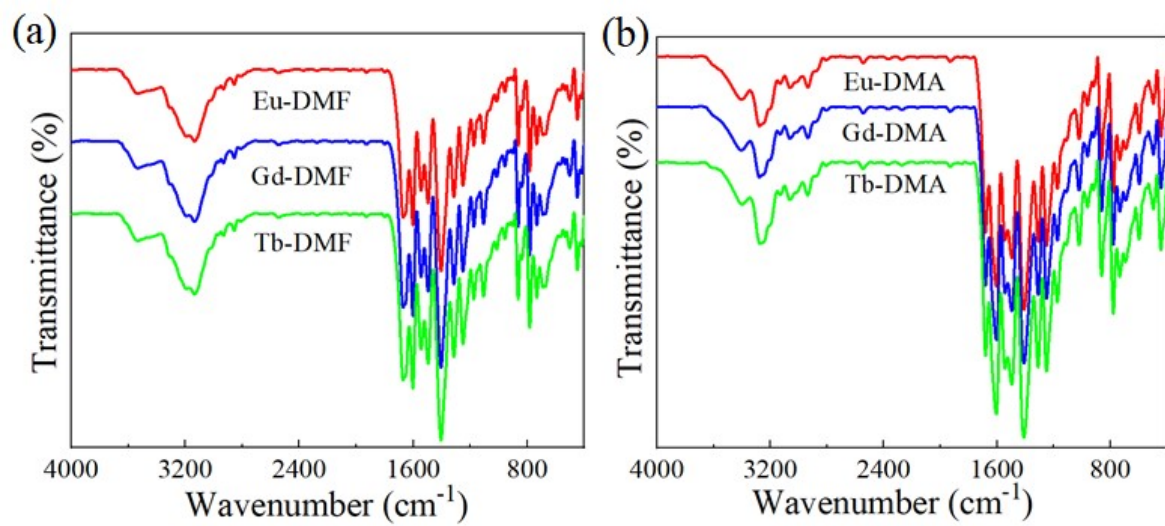


Fig. S1. IR spectra of **Ln-DMF** (a) and **Ln-DMA** (b).

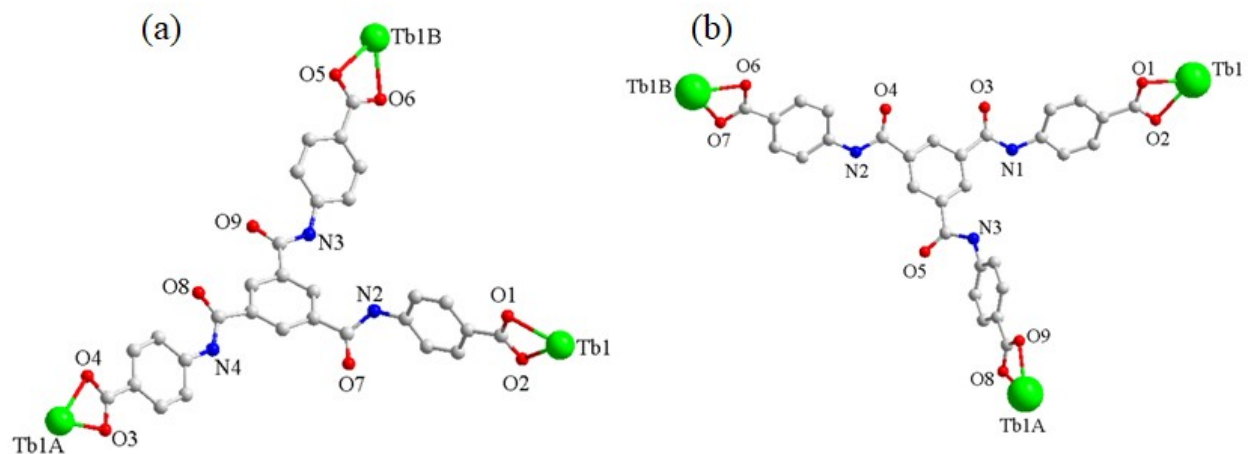


Fig. S2. Coordination modes of the H_3L ligand in **Tb-DMF** (a) and **Tb-DMA** (b).

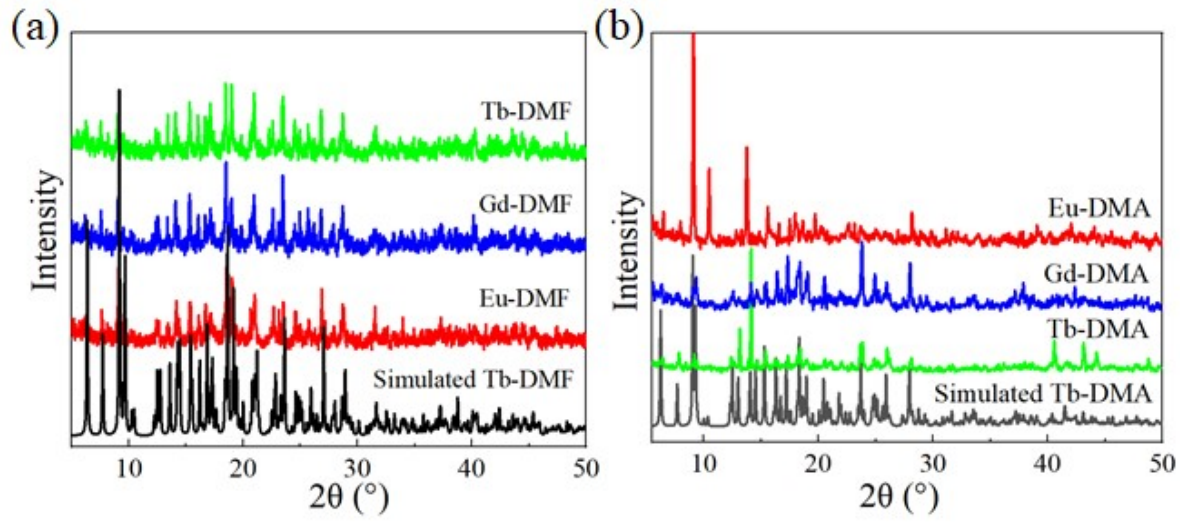


Fig. S3. PXRD patterns of **Ln-DMF** (a) and **Ln-DMA** (b).

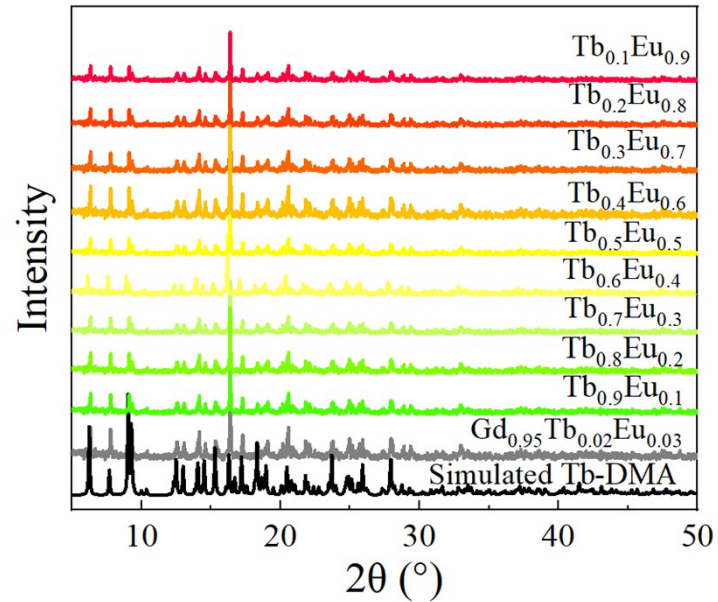


Fig. S4. PXRD patterns of **Eu_xTb_{1-x}-DMA** and **Gd_{0.95}Tb_{0.02}Eu_{0.03}-DMA**.

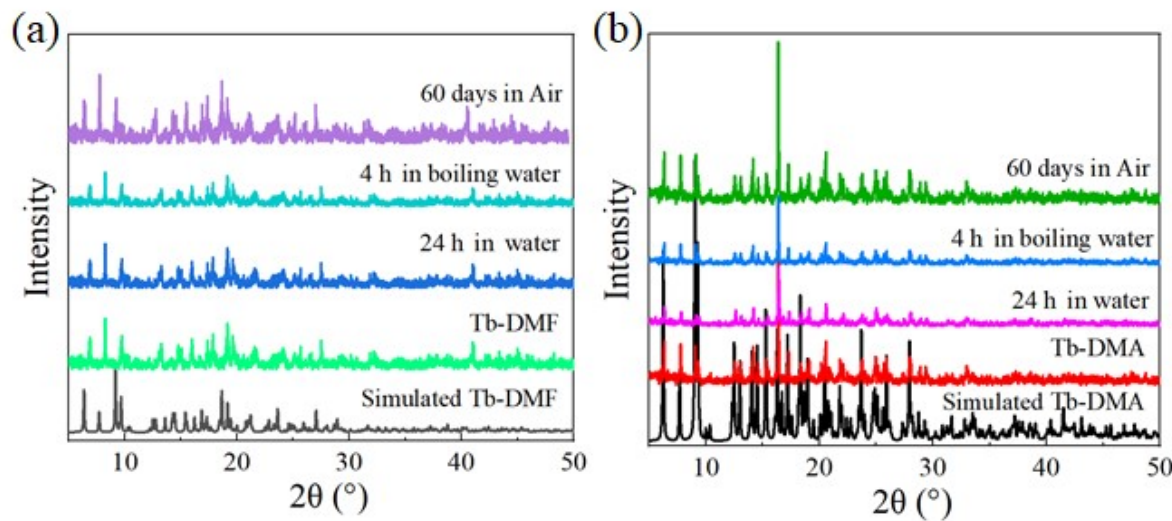


Fig. S5. PXRD patterns of **Tb-DMF** (a) and **Tb-DMA** (b) soaked in boiling water for 4 h and soaked in water for 24 h and exposed to air for 60 d.

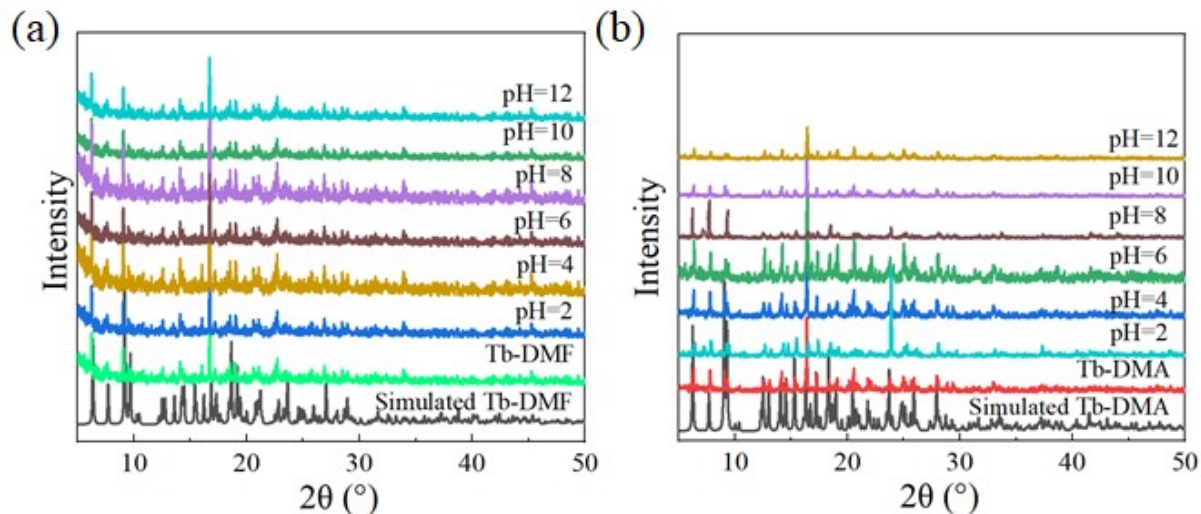


Fig. S6. PXRD patterns of **Tb-DMF** (a) and **Tb-DMA** (b) soaked in water solution with different pH for 10 h.

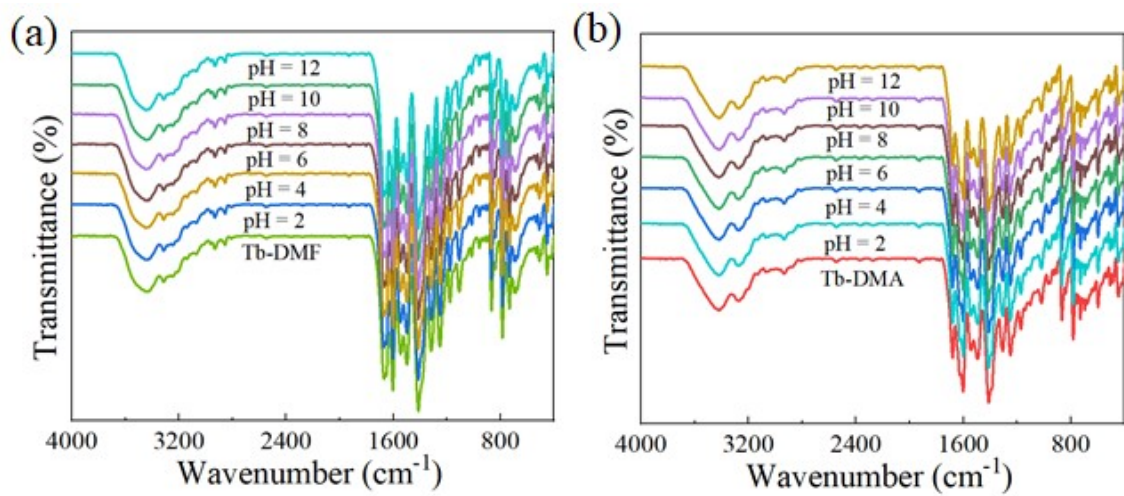


Fig. S7. FT-IR spectra of **Tb-DMF** (a) and **Tb-DMA** (b) soaked in water solution with different pH for 10 h.

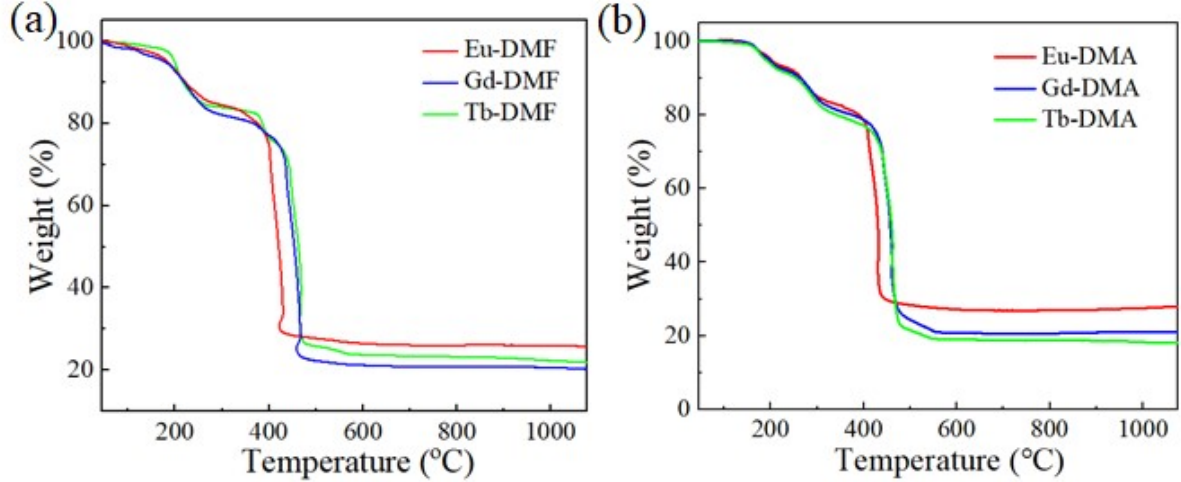


Fig. S8. TG curves of **Ln-DMF** (a) and **Ln-DMA** (b).

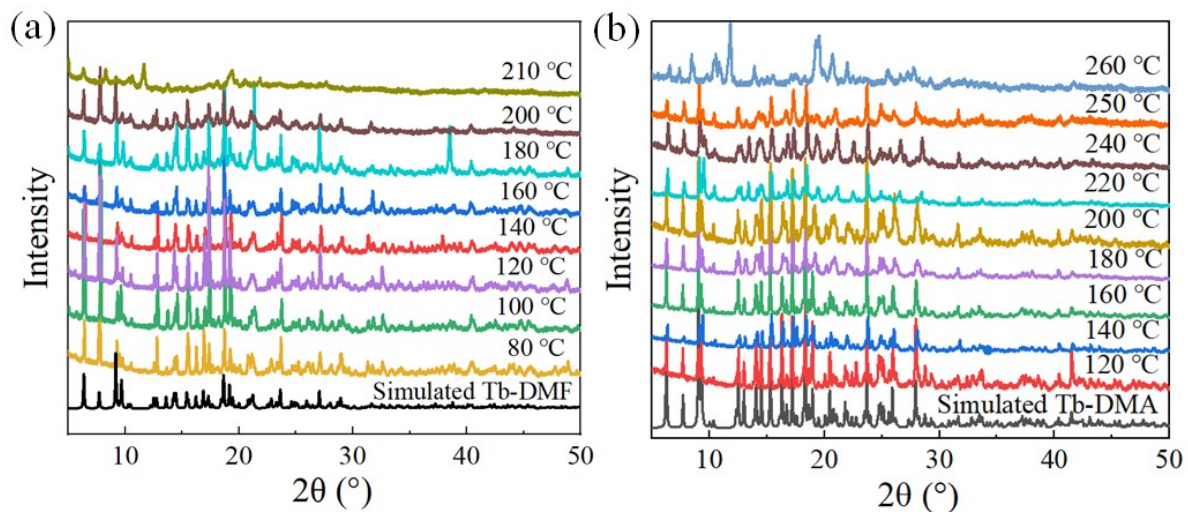


Fig. S9. PXRD patterns of Tb-DMF (a) and Tb-DMA (b) under different temperatures.

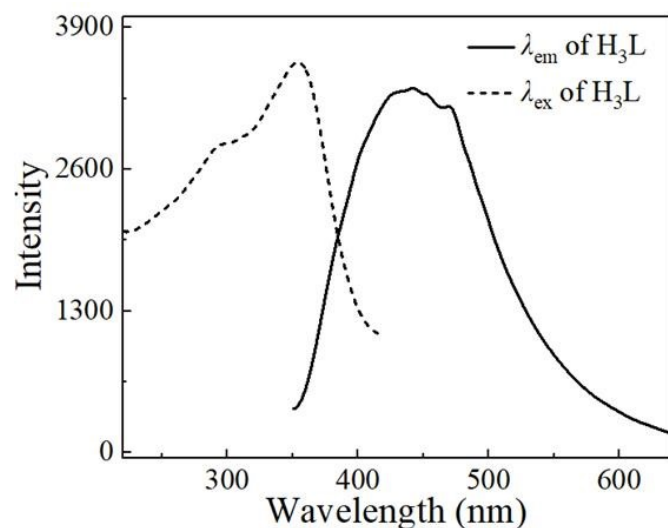


Fig. S10. Solid-state luminescent spectra of H_3L .

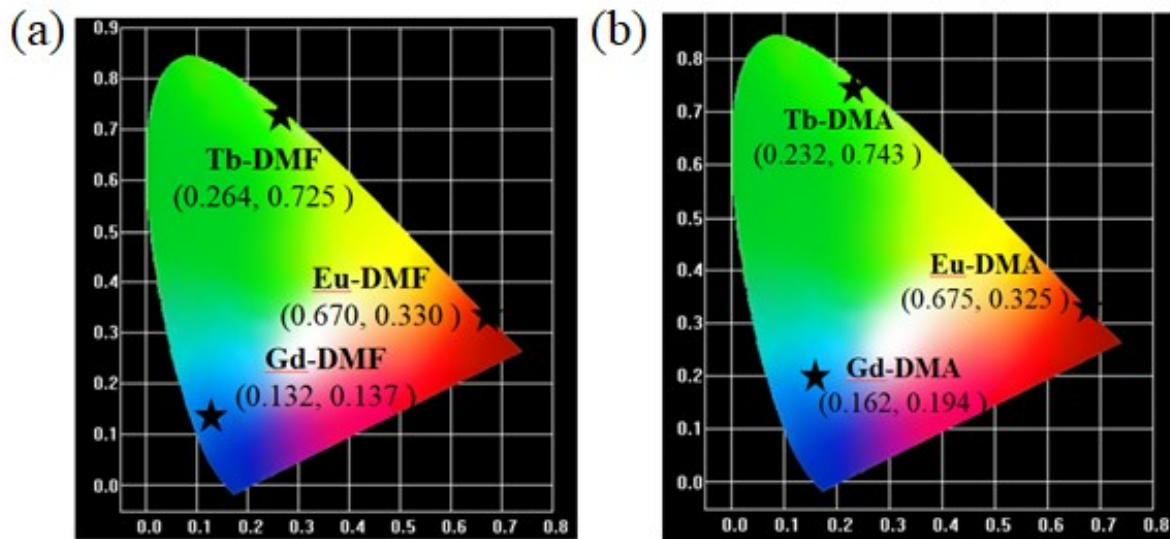


Fig. S11. CIE chromaticity diagrams of **Ln-DMF** (a) and **Ln-DMA** (b).

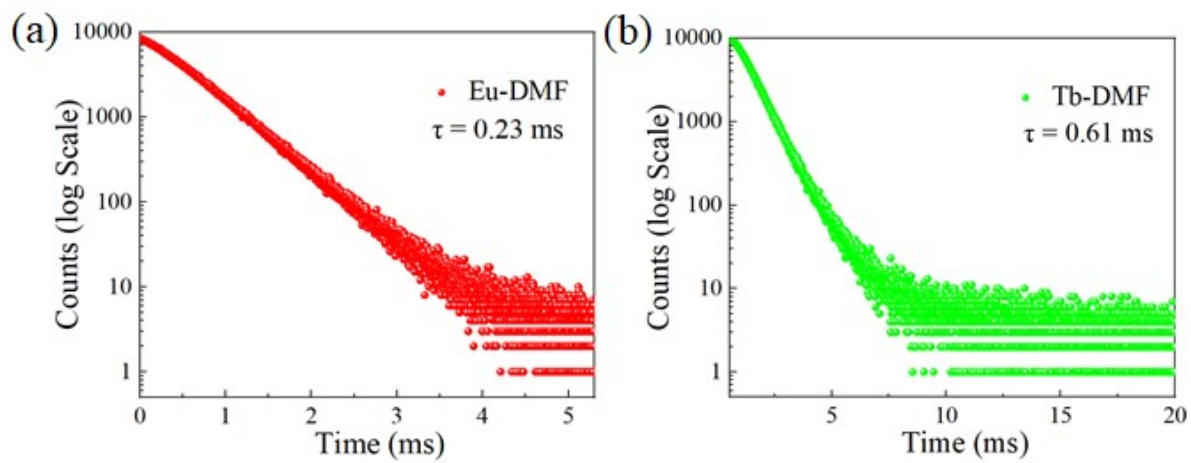


Fig. S12. Solid-state fluorescence decay curves of **Eu-DMF** (a) and **Tb-DMF** (b).

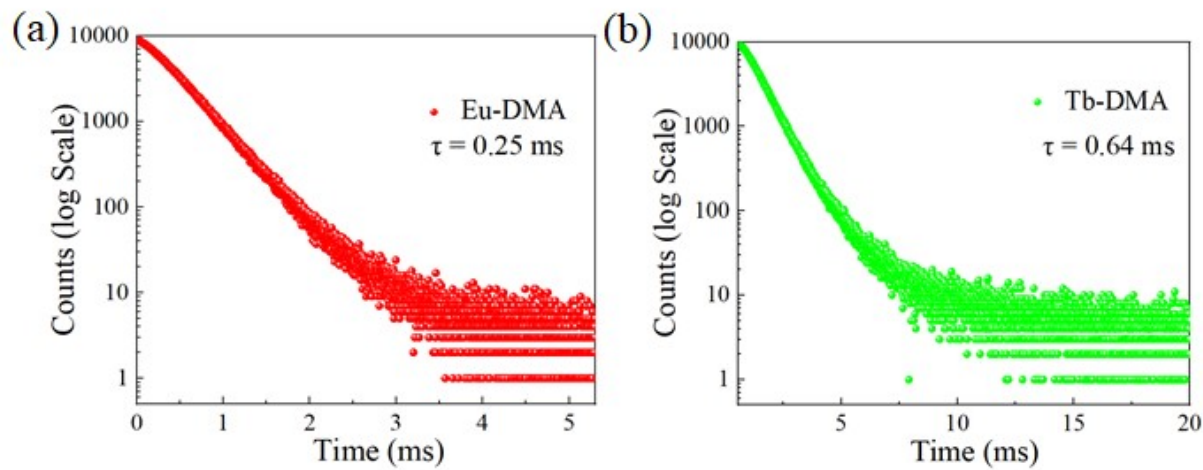


Fig. S13. Solid-state fluorescence decay curves of Eu-DMA (a) and Tb-DMA (b).

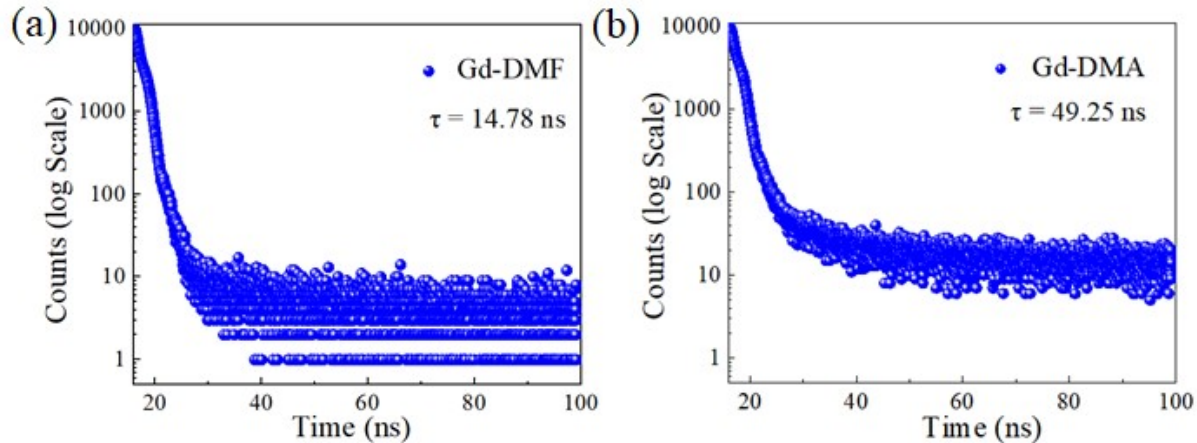


Fig. S14. Solid-state fluorescence decay curves of Gd-DMF (a) and Gd-DMA (b).

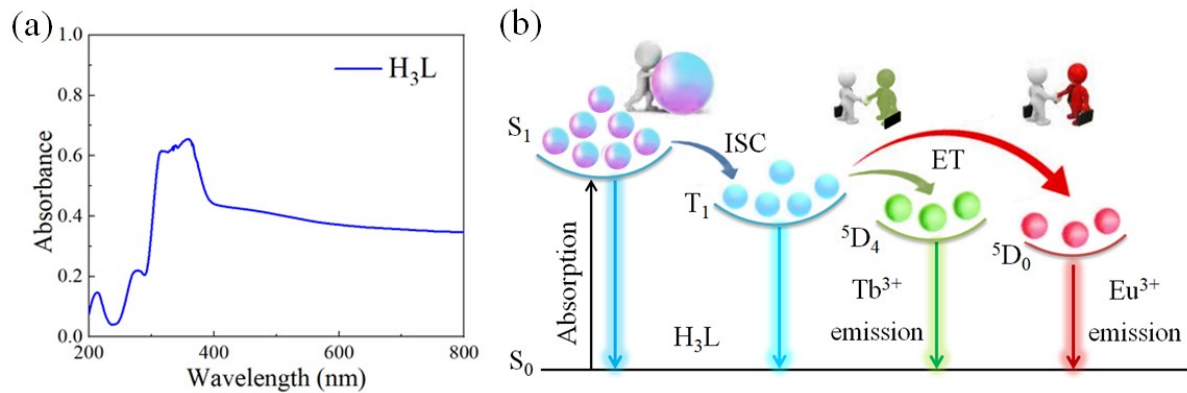


Fig. S15. (a) UV–Vis absorption spectrum of H_3L ; (b) Diagram of energy transfer process in **Ln-DMF** and **Ln-DMA**.

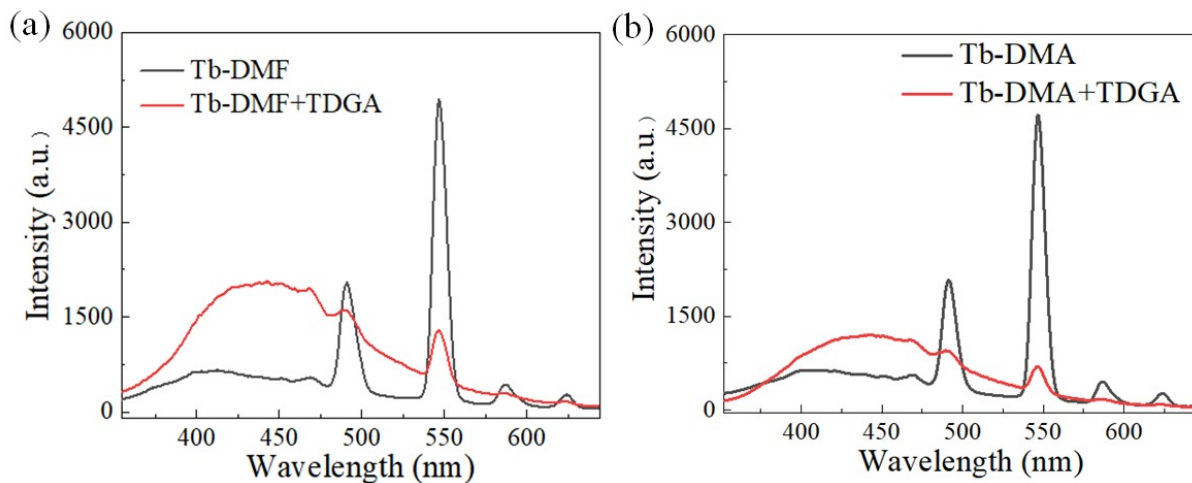


Fig. S16. The emission spectra of **Tb-DMF**, **Tb-DMF+TDGA** (a) and **Tb-DMA**, **Tb-DMA+TDGA** (b).

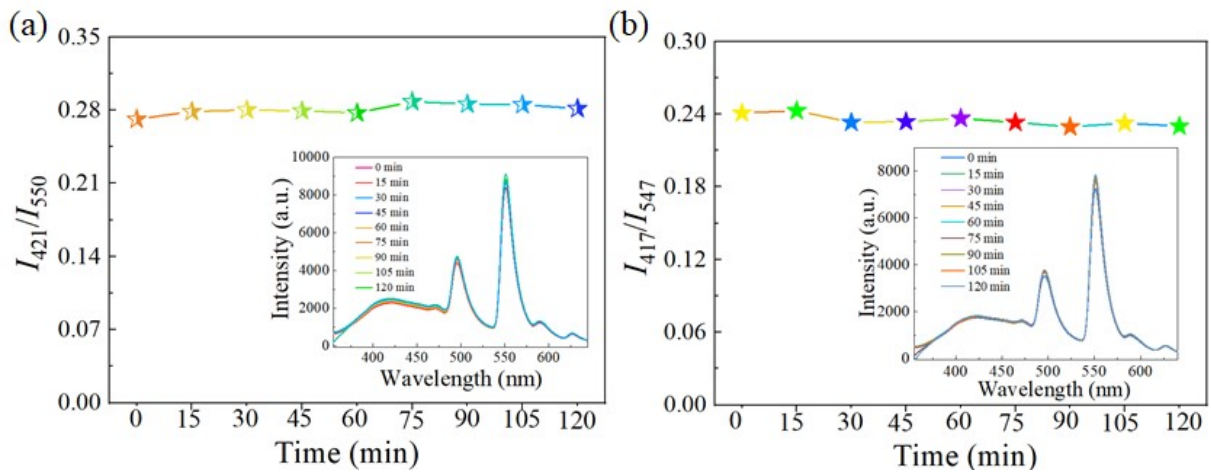


Fig. S17. Time-dependent luminescence intensity ratios (I_{421}/I_{550} , I_{417}/I_{547}) for **Tb-DMF** (a) and **Tb-DMA** (b) in water solution.

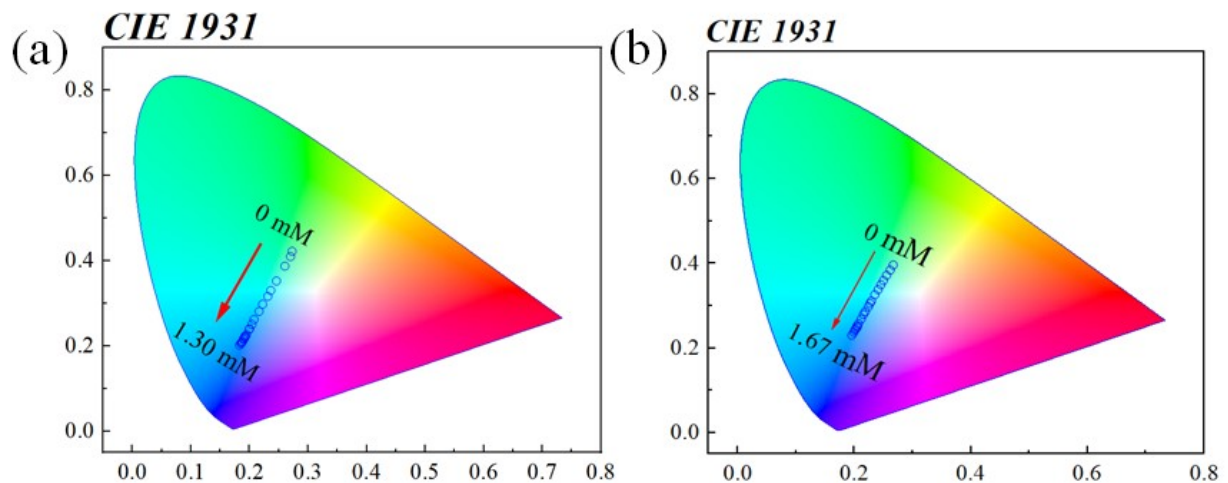


Fig. S18. CIE chromaticity diagram showing the variations of fluorescent color coordinates of **Tb-DMF** (a) and **Tb-DMA** (b) dispersions in different TDGA concentrations.

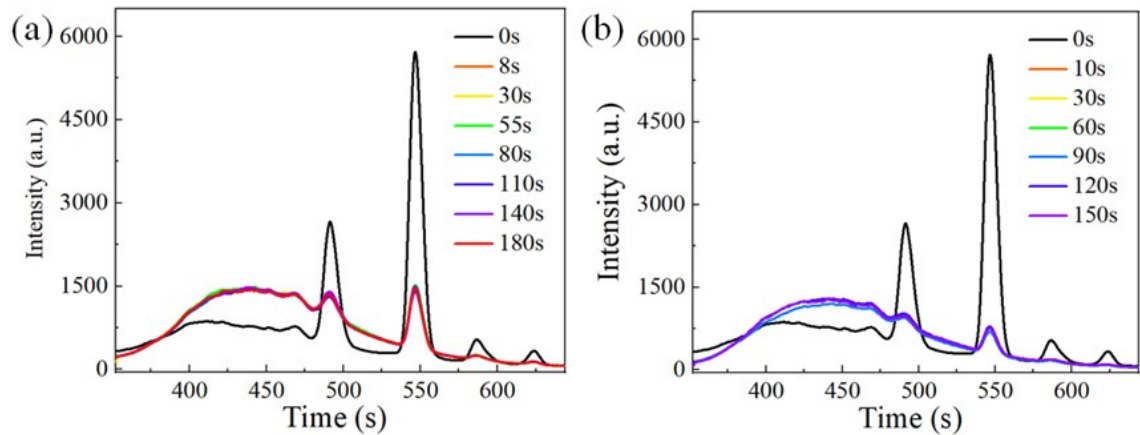


Fig. S19. Luminescent spectra of **Tb-DMF** (a) and **Tb-DMA** (b) after the addition of TDGA at different times.

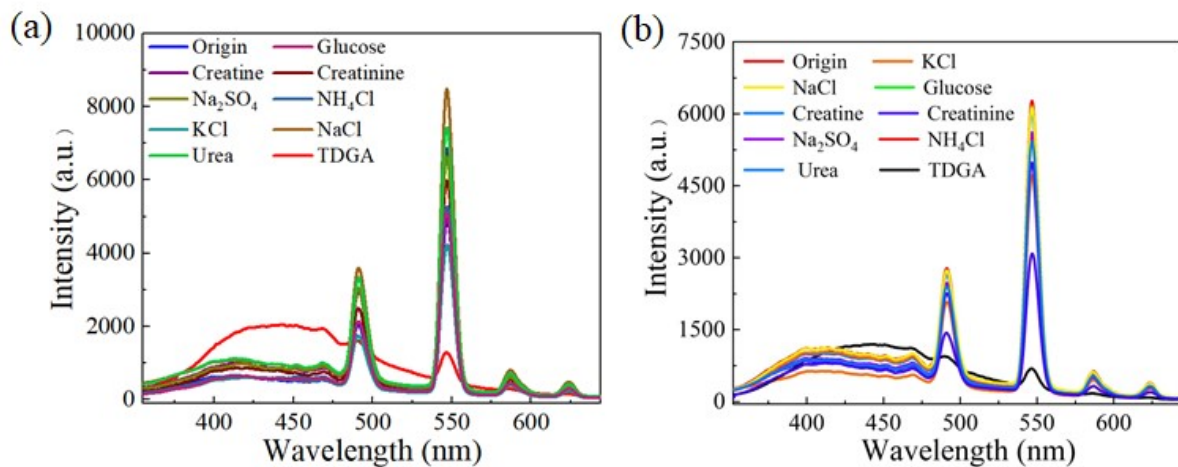


Fig. S20. Luminescent spectra of **Tb-DMF** (a) and **Tb-DMA** (b) suspensions with various urine components.

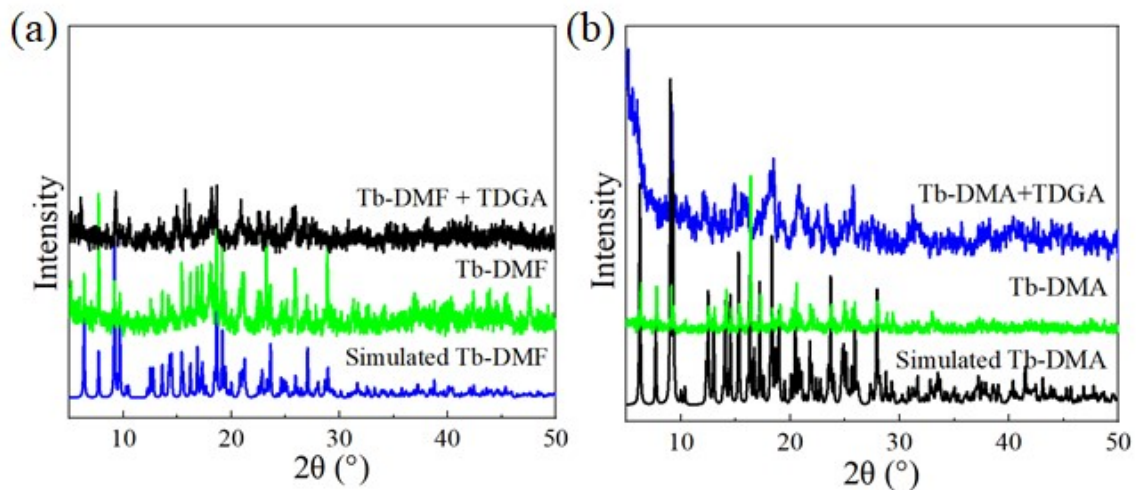


Fig. S21. PXRD patterns of Tb-DMF (a) and Tb-DMA (b) before and after detection of TDGA.

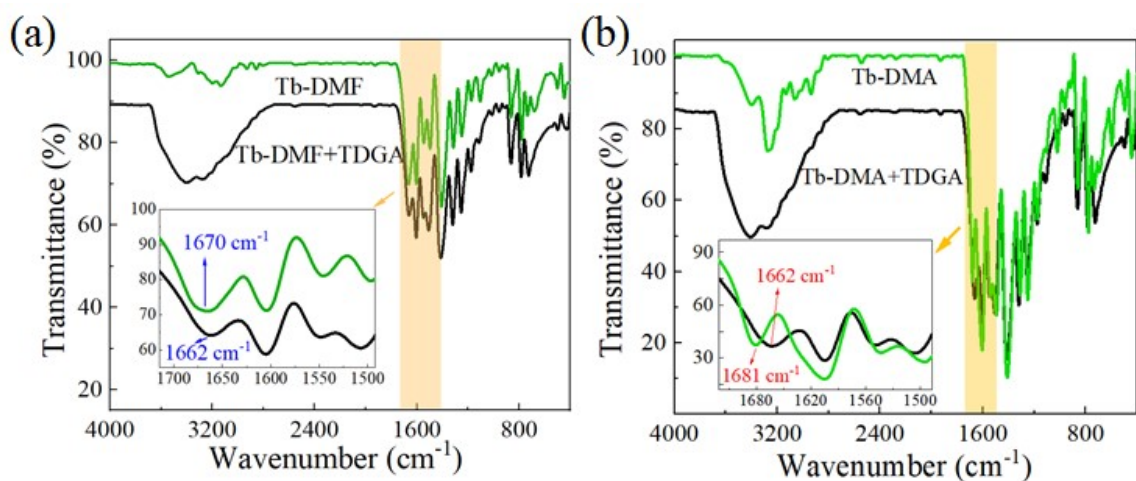


Fig. S22. FT-IR spectra of Tb-DMF (a) and Tb-DMA (b) before and after detection of TDGA.

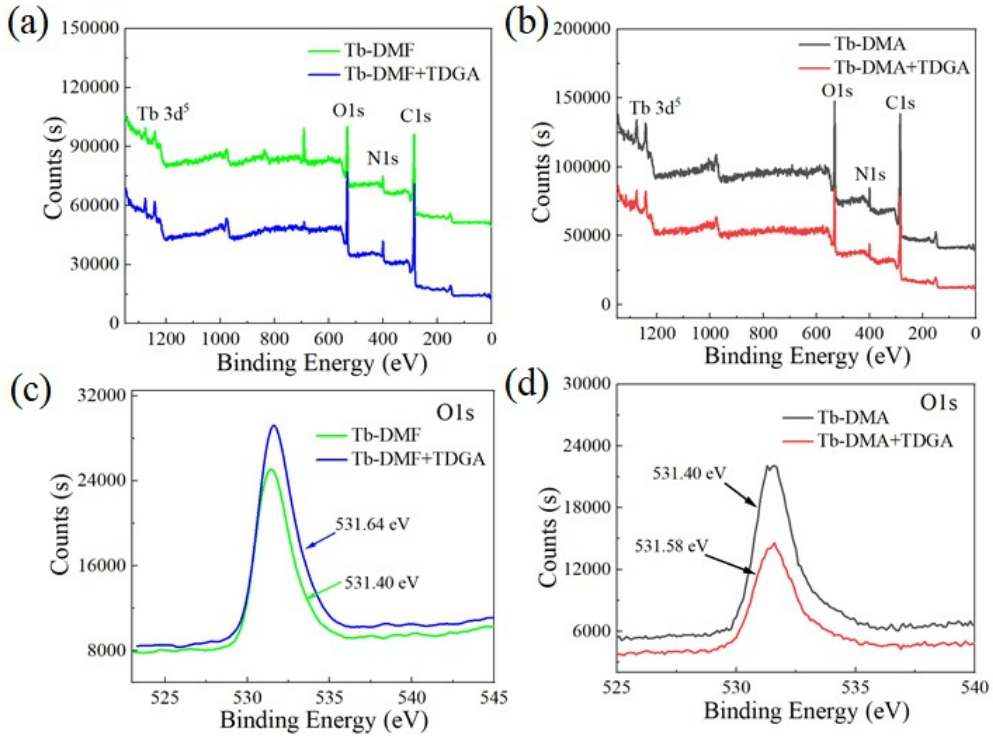


Fig. S23. The full XPS spectra and O1s XPS of **Tb-DMF** (a, c) and **Tb-DMA** (b, d).

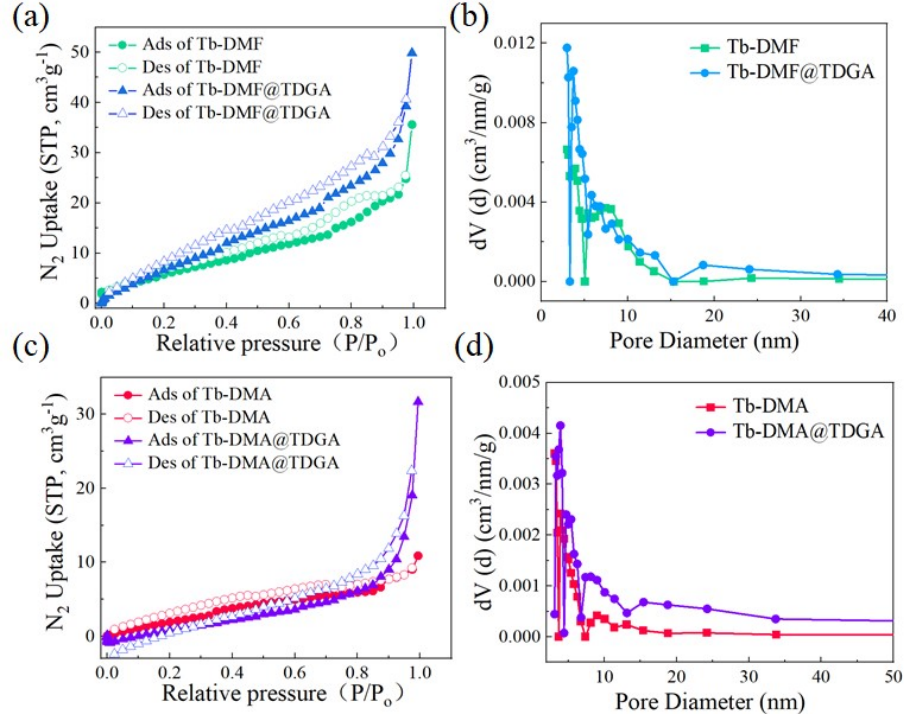


Fig. S24. (a, c) N₂ adsorption and desorption isotherms at 77 K of the **Tb-DMF/Tb-DMA** samples before and after sensing TDGA; (b, d) Pore size distribution curves of **Tb-DMF/Tb-DMA** samples before and after sensing TDGA based on N₂ adsorption isotherms at 77 K.

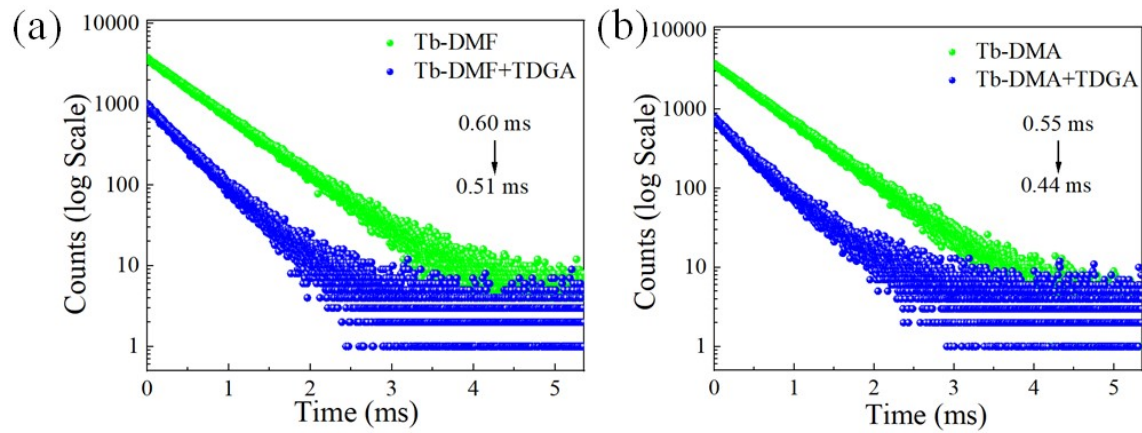


Fig. S25. Emission decay profiles of **Tb-DMF** (a) and **Tb-DMA** (b) suspensions before and after detection of TDGA.

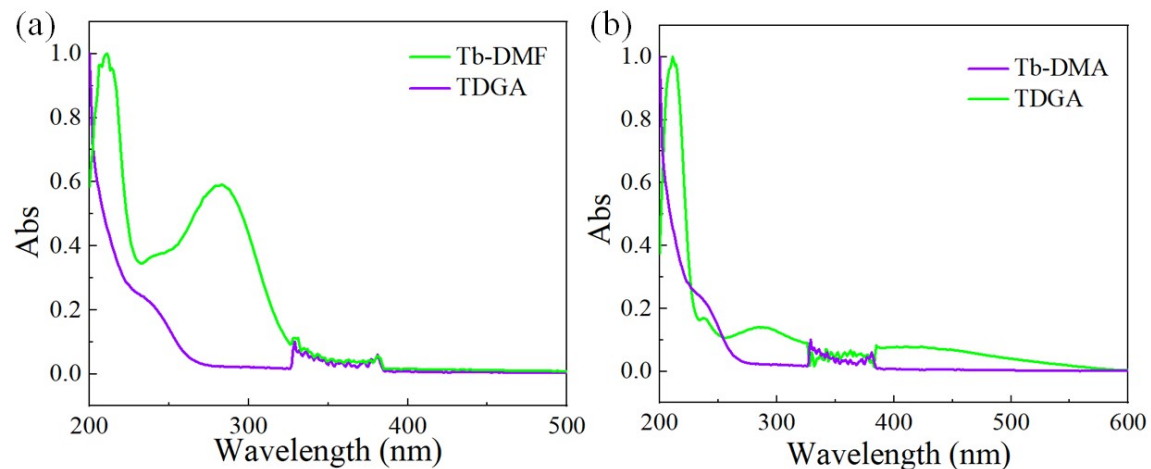


Fig. S26. UV-Vis absorption spectra of TDGA, **Tb-DMF** (a) and **Tb-DMA** (b) in aqueous solutions

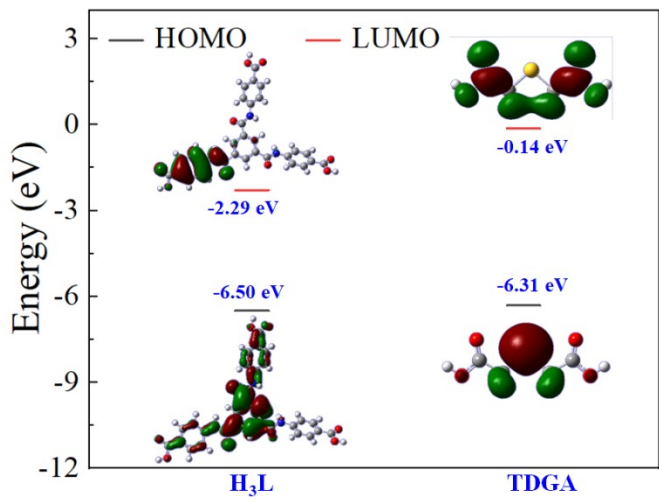


Fig. S27. HOMO and LUMO energy levels of the TDGA and the H_3L ligand calculated by density functional theory (DFT) at B3LYP/6–31G (d, p) basis set.

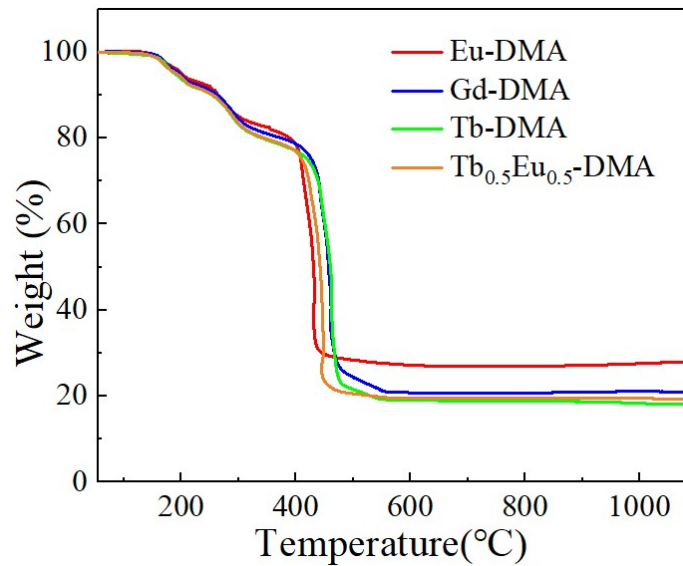


Fig. S28. TG curves of Ln -DMA and $\text{Tb}_{0.5}\text{Eu}_{0.5}$ -DMA.

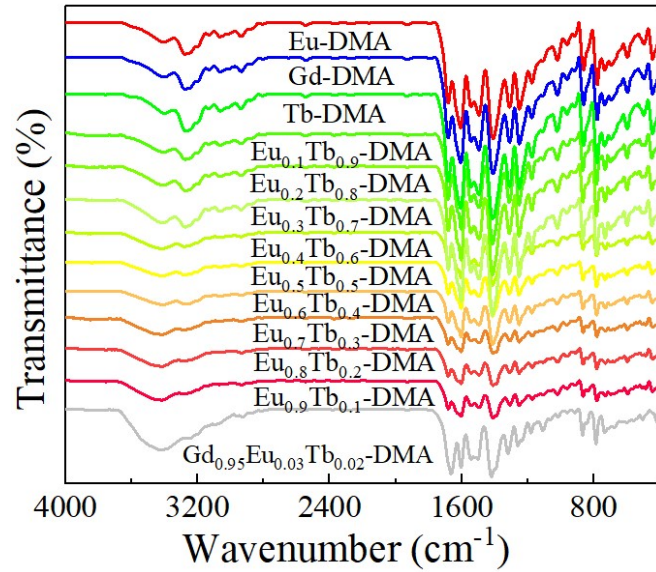


Fig. S29. FT-IR spectra of $\text{Eu}_x\text{Tb}_{1-x}\text{-DMA}$ and $\text{Gd}_{0.95}\text{Eu}_{0.03}\text{Tb}_{0.02}\text{-DMA}$.

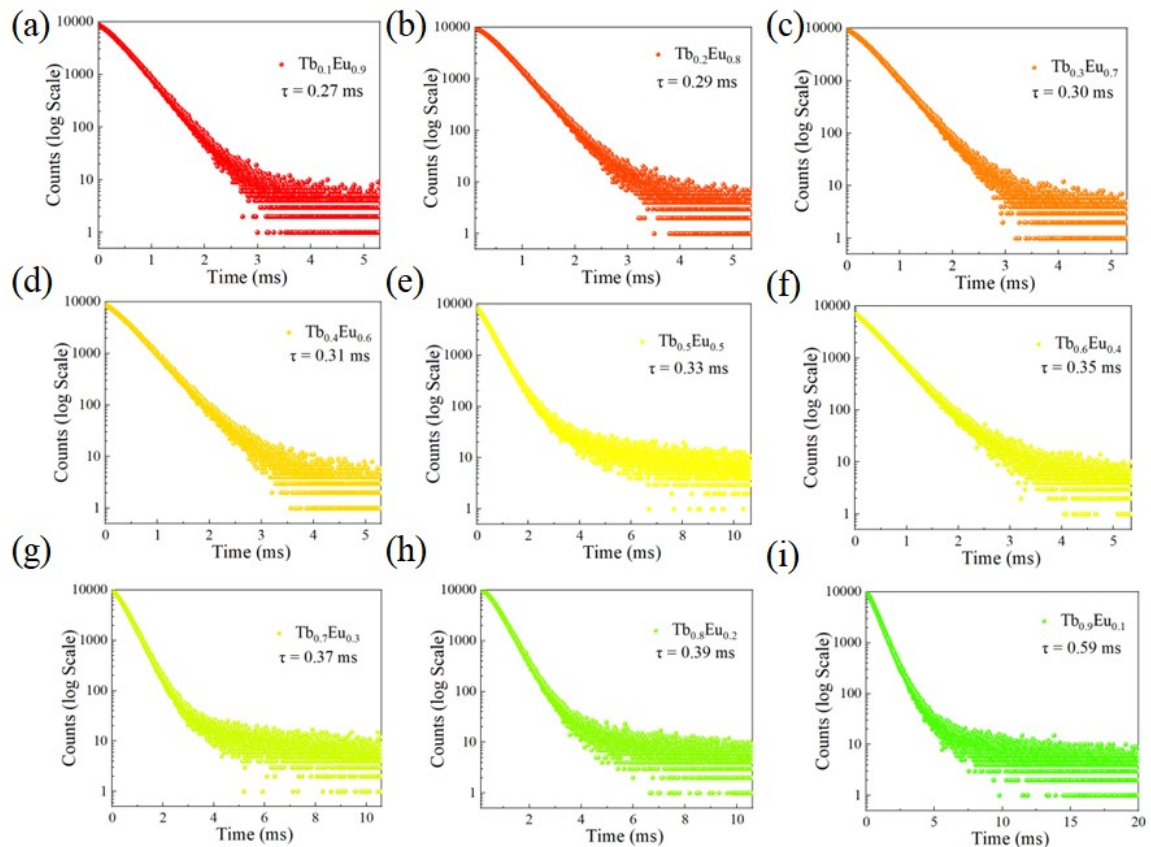


Fig. S30. Emission decay profiles of $\text{Eu}_x\text{Tb}_{1-x}\text{-DMA}$.

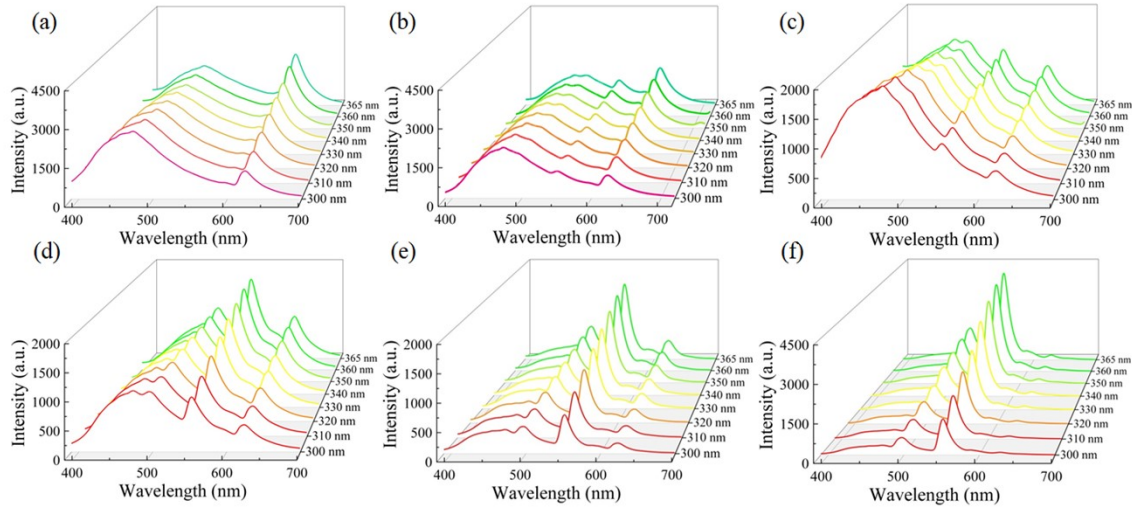


Fig. S31. Luminescent emission spectra of **Eu-DMA** (a), **Eu_{0.8}Tb_{0.2}-DMA** (b), **Eu_{0.6}Tb_{0.4}-DMA** (c), **Eu_{0.4}Tb_{0.6}-DMA** (d), **Eu_{0.2}Tb_{0.8}-DMA** (e), and **Tb-DMA** (f) under different excitation wavelengths.

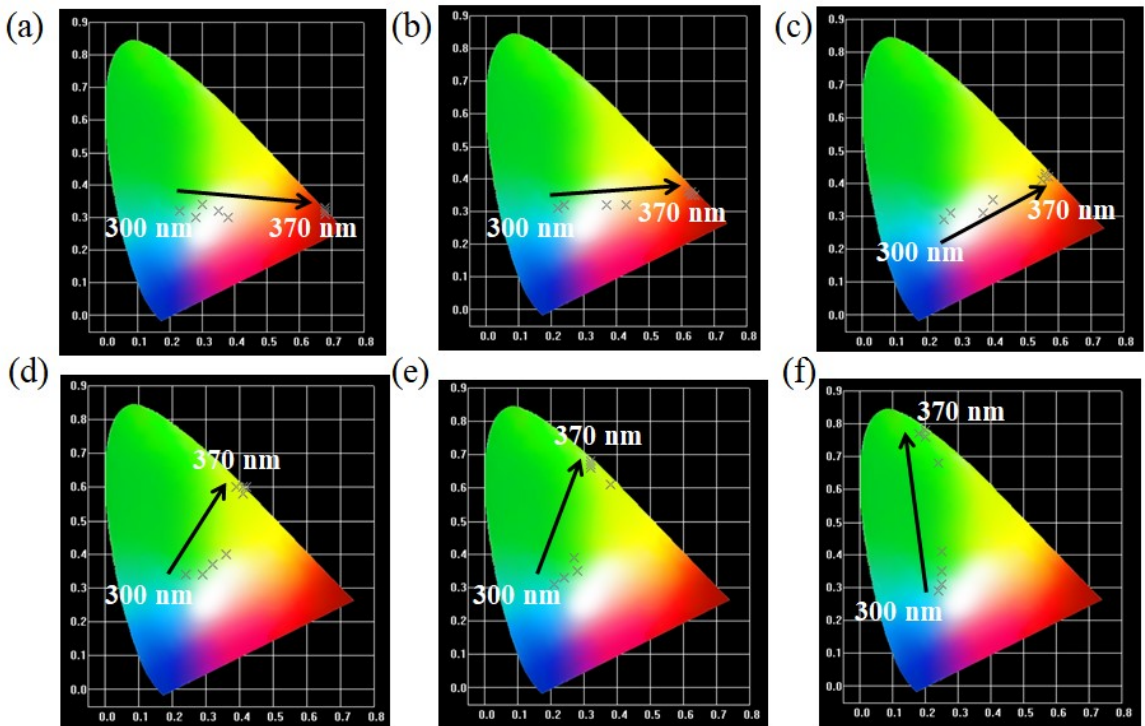


Fig. S32. CIE chromaticity diagrams showing the variation of fluorescent color coordinates of **Eu-DMA** (a), **Eu_{0.8}Tb_{0.2}-DMA** (b), **Eu_{0.6}Tb_{0.4}-DMA** (c), **Eu_{0.4}Tb_{0.6}-DMA** (d), **Eu_{0.2}Tb_{0.8}-DMA** (e), and **Tb-DMA** (f) under different excitation wavelengths.

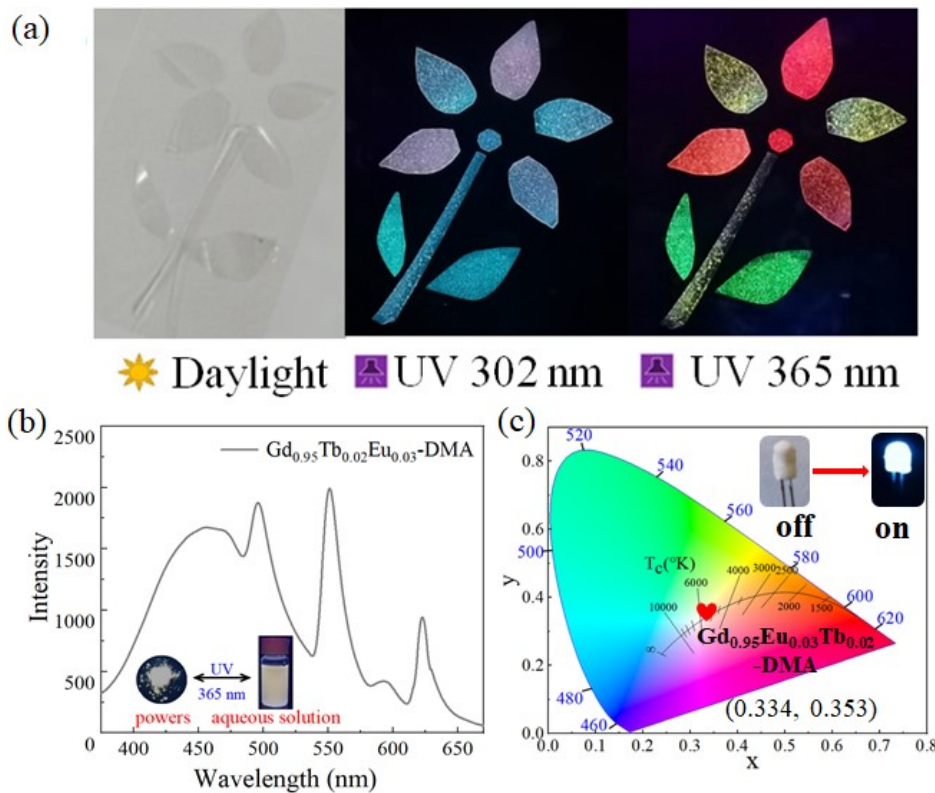


Fig.S33. (a) Photographs of flower using different colors of $\text{Eu}_x\text{Tb}_{1-x}$ -DMA@PMMA composites under daylight, 302 nm and 365 nm UV lamp; (b) Luminescent emission spectrum (inset, photographs of powder and aqueous solution of $\text{Gd}_{0.95}\text{Tb}_{0.02}\text{Eu}_{0.03}$ -DMA; (c) CIE chromaticity diagram of $\text{Gd}_{0.95}\text{Eu}_{0.03}\text{Tb}_{0.02}$ -DMA under 365 nm UV light (inset, image of $\text{Gd}_{0.95}\text{Eu}_{0.03}\text{Tb}_{0.02}$ -DMA led device).

Table S1. Crystal data and structure refinements for **Ln-DMF**.

Compounds	Eu-DMF	Gd-DMF	Tb-DMF
Empirical formula	C ₃₆ H ₃₄ N ₅ O ₁₂ Eu	C ₃₆ H ₃₄ N ₅ O ₁₂ Gd	C ₃₆ H ₃₄ N ₅ O ₁₂ Tb
Formula weight	880.64	885.93	887.60
Crystal system	Triclinic	Triclinic	Triclinic
Space group	<i>P</i> 	<i>P</i> 	<i>P</i> 
<i>a</i> /Å	10.9021(7)	10.8833(10)	10.8696(2)
<i>b</i> /Å	12.5315(8)	12.5173(12)	12.5017(2)
<i>c</i> /Å	14.4609(10)	14.4227(13)	14.3804(2)
$\alpha/^\circ$	88.9970(10)	89.161(2)	89.0640(10)
$\beta/^\circ$	75.3580(10)	75.3020(10)	75.440(2)
$\gamma/^\circ$	66.8780(10)	66.9750(10)	66.740(2)
<i>V</i> /Å ³	1750.5(2)	1741.2(3)	1730.07(6)
<i>Z</i>	2	2	2
$\rho_{\text{calc}} \text{g/cm}^3$	1.671	1.690	1.704
μ/mm^{-1}	1.865	1.978	2.118
Reflections collected	10647	10232	32233
Independent reflections	7449 [$R_{\text{int}} = 0.0217$]	7084 [$R_{\text{int}} = 0.0252$]	9124 [$R_{\text{int}} = 0.0389$]
Goodness of fit on F^2	1.018	1.020	1.053
[^a] R_I , wR_2 [$I > 2\sigma(I)$]	0.0359, 0.0721	0.0390, 0.0705	0.0242, 0.0615
[^a] R_1 , wR_2 (all data)	0.0502, 0.0776	0.0554, 0.0761	0.0267, 0.0626

[^a] $R_I = \sum (|F_0| - |F_C|) / \sum |F_0|$; $wR_2 = [\sum w (|F_0| - |F_C|)^2 / \sum w F_0^2]^{1/2}$

Table S2. Selected bond lengths (\AA) and angles ($^\circ$) for **Tb-DMF**.

Tb1–O4#1	2.4121(16)	O10–Tb1–O2	131.68(6)
Tb1–O3#1	2.3981(15)	O10–Tb1–O6#2	131.22(7)
Tb1–O1	2.3670(16)	O10–Tb1–O5#2	92.29(7)
Tb1–O2	2.4612(16)	O10–Tb1–O11	71.41(6)
Tb1–O10	2.3213(19)	O6#2–Tb1–O4#1	135.38(6)
Tb1–O6#2	2.3761(15)	O6#2–Tb1–O3#1	81.18(5)
Tb1–O5#2	2.3861(17)	O6#2–Tb1–O2	83.93(6)
Tb1–O11	2.3781(16)	O6#2–Tb1–O5#2	55.17(6)
O4#1–Tb1–O2	89.27(6)	O6#2–Tb1–O11	77.71(6)
O3#1–Tb1–O4#1	54.21(5)	O5#2–Tb1–O4#1	166.30(7)
O3#1–Tb1–O2	82.93(6)	O5#2–Tb1–O3#1	135.23(6)
O1–Tb1–O4#1	84.51(6)	O5#2–Tb1–O2	83.05(7)
O1–Tb1–O3#1	121.50(6)	O11–Tb1–O4#1	94.00(7)
O1–Tb1–O2	54.04(6)	O11–Tb1–O3#1	80.54(6)
O1–Tb1–O6#2	123.94(6)	O11–Tb1–O2	156.91(6)
O1–Tb1–O5#2	81.79(7)	O11–Tb1–O5#2	97.51(7)
O1–Tb1–O11	149.02(6)	C25–O4–Tb1#3	92.93(13)
O10–Tb1–O4#1	84.34(7)	C25–O3–Tb1#3	93.18(13)
O10–Tb1–O3#1	127.79(7)	C33–O6–Tb1#4	92.87(13)
O10–Tb1–O1	77.66(6)	C33–O5–Tb1#4	91.90(13)

Symmetry transformations used to generate equivalent atoms: #1 1+x, 1+y, +z; #2 -1+x, 1+y, 1+z; #3 -1+x, -1+y, +z; #4 1+x, -1+y, -1+z.

Table S3. Crystal data and structure refinements for **Ln-DMA**.

Compounds	Eu-DMA	Gd-DMA	Tb-DMA
Empirical formula	C ₃₈ H ₃₈ N ₅ O ₁₂ Eu	C ₃₈ H ₃₈ N ₅ O ₁₂ Gd	C ₃₈ H ₃₈ N ₅ O ₁₂ Tb
Formula weight	908.69	913.98	915.65
Crystal system	Triclinic	Triclinic	Triclinic
Space group	<i>P</i> 	<i>P</i> 	<i>P</i> 
<i>a</i> /Å	11.1492(10)	11.1418(10)	11.1070(6)
<i>b</i> /Å	12.5031(12)	12.4730(12)	12.4752(7)
<i>c</i> /Å	14.8728(14)	14.8926(14)	14.8652(8)
<i>α</i> /°	88.1470(10)	88.0870(10)	88.3540(10)
<i>β</i> /°	72.7660(10)	72.7110(10)	72.8610(10)
<i>γ</i> /°	67.4740(10)	67.4860(10)	67.5570(10)
<i>V</i> /Å ³	1821.3(3)	1817.9(3)	1811.00(17)
<i>Z</i>	2	2	2
ρ _{calc} g/cm ³	1.657	1.670	1.679
μ/mm ⁻¹	1.795	1.898	2.026
Reflections collected	11930	10493	11913
Independent reflections	8545 [R _{int} = 0.0268]	7227 [R _{int} = 0.0250]	8543 [R _{int} = 0.0182]
Goodness of fit on <i>F</i> ²	1.024	1.025	1.024
[^a]R ₁ , wR ₂ [<i>I</i> >2σ(<i>I</i>)]	0.0466, 0.0888	0.0445, 0.0951	0.0391, 0.0893
[^a]R ₁ , wR ₂ (all data)	0.0678, 0.0972	0.0630, 0.1035	0.0494, 0.0944

[^a] R₁ = Σ (|F₀| - |F_C|) / Σ |F₀|; wR₂ = [Σ w (|F₀| - |F_C|)² / Σ w F₀²]^{1/2}

Table S4. Selected bond lengths (\AA) and angles ($^\circ$) for **Tb-DMA**.

Tb1–O8#1	2.488(3)	O7#2–Tb1–O11	81.90(10)
Tb1–O2	2.432(3)	O11–Tb1–O8#1	78.39(9)
Tb1–O6#2	2.406(3)	O11–Tb1–O2	77.11(12)
Tb1–O9#1	2.390(3)	O1–Tb1–O8#1	153.12(11)
Tb1–O7#2	2.409(3)	O1–Tb1–O2	77.97(11)
Tb1–O11	2.412(3)	O1–Tb1–O6#2	87.14(12)
Tb1–O1	2.364(3)	O1–Tb1–O9#1	54.27(10)
Tb1–O10	2.294(3)	O1–Tb1–O7#2	173.30(11)
O2–Tb1–O8#1	89.90(11)	O1–Tb1–O11	90.92(12)
O6#2–Tb1–O8#1	26.75(10)	O10–Tb1–O8#1	132.51(10)
O6#2–Tb1–O2	81.53(10)	O10–Tb1–O2	94.75(13)
O6#2–Tb1–O7#2	95.68(12)	O10–Tb1–O6#2	131.20(11)
O6#2–Tb1–O11	132.11(10)	O10–Tb1–O9#1	132.06(12)
O9#1–Tb1–O8#1	54.06(10)	O10–Tb1–O7#2	84.65(12)
O9#1–Tb1–O2	85.48(13)	O10–Tb1–O11	78.21(11)
O9#1–Tb1–O6#2	53.27(10)	O10–Tb1–O1	131.74(12)
O9#1–Tb1–O7#2	125.53(10)	O6–C22–Tb1#4	59.92(19)
O9#1–Tb1–O11	85.95(12)	C7–C22–Tb1#4	60.08(19)
O7#2–Tb1–O8#1	117.21(11)	O8–C30–Tb1#3	62.5(2)
O7#2–Tb1–O2	153.15(11)	O9–C30–Tb1#3	58.0(2)

Symmetry transformations used to generate equivalent atoms: #1 1+x, -1+y, -1+z; #2 2+x, +y, -1+z; #3 -1+x, 1+y, 1+z; #4 -2+x, +y, 1+z.

Table S5. Comparison of the proposed sensor for TDGA detection with other methods.

Sensing Method	Material	K_{sv}/M^{-1}	LOD/ μM	Visual detection	Ref.
Fluorescence	$\text{Ln}(\text{NO}_3)_3 \cdot 6\text{H}_2\text{O}$	2.99×10^3	1.7	Yes	6
Fluorescence	$\text{Cu}^{2+}-\text{Eu}^{3+}-\text{Zr}^{4+}-\text{MOF}$	—	13.36	—	7
Fluorescence	$\text{C}460@\text{Tb}-\text{UiO}-66-(\text{COOH})_2$	—	77.78	No	8
Fluorescence	$\text{Eu}-\text{CBO}@\text{UiO}-66$	—	0.34	Yes	9
Fluorescence	$\text{DPA/Eu}@\text{PY-DHPB COF-COOH}$	—	0.078	Yes	10
RSLC-S-MS	—	—	0.33	—	11
Voltammetric	—	—	1.07	—	12
Double Ratiometric Fluorescence	Tb-DMF	5.30×10^3 6.34×10^3	0.43, 0.34	Yes	This work
Double Ratiometric Fluorescence	Tb-DMA	1.68×10^3 1.84×10^3	1.34, 1.22	Yes	This work

Table S6. Determination of TDGA with Tb-DMF in simulated urine samples by standard addition method.

Samples	Added (mM)	Funded (mM)	<i>RSD (%)</i>	Recovery (%)
			$(I_{421\text{nm}}/I_{550\text{nm}}, I_{452\text{nm}}/I_{550\text{nm}})$	$(I_{421\text{nm}}/I_{550\text{nm}}, I_{452\text{nm}}/I_{550\text{nm}})$
Simulated Urine	2.50	2.52, 2.58	2.73%, 0.82%	98.94%, 96.63%
	4.98	4.84, 4.88	0.21%, 5.39%	102.75%, 101.88%
	9.90	9.71, 9.64	0.62%, 0.09%	101.99%, 102.66%

Table S7. Determination of TDGA with Tb-DMA in simulated urine samples by standard addition method.

Samples	Added (mM)	Funded (mM)	RSD (%)	Recovery (%)
		$(I_{421\text{nm}}/I_{550\text{nm}},$ $I_{452\text{nm}}/I_{550\text{nm}})$	$(I_{421\text{nm}}/I_{550\text{nm}},$ $I_{452\text{nm}}/I_{550\text{nm}})$	$(I_{421\text{nm}}/I_{550\text{nm}},$ $I_{452\text{nm}}/I_{550\text{nm}})$
Simulated Urine	4.98	5.16, 4.72	1.65%, 5.36%	96.34%, 110.75%
	9.90	9.20, 10.03	1.14%, 1.00%	107.64%, 98.70%
	19.61	18.25, 17.70	3.71%, 5.36%	107.41%, 105.35%

Table S8. Determination of TDGA with Tb-DMF in real urine samples by standard addition method.

Samples	Added (mM)	Funded (mM)	RSD (%)	Recovery (%)
		$(I_{421\text{nm}}/I_{550\text{nm}},$ $I_{452\text{nm}}/I_{550\text{nm}})$	$(I_{421\text{nm}}/I_{550\text{nm}},$ $I_{452\text{nm}}/I_{550\text{nm}})$	$(I_{421\text{nm}}/I_{550\text{nm}},$ $I_{452\text{nm}}/I_{550\text{nm}})$
Real Urine	2.50	2.58, 2.33	0.48%, 0.14%	96.65%, 107.27%
	4.98	4.89, 4.84	0.29%, 0.09%	101.84%, 102.77%
	9.90	9.68, 9.87	0.05%, 0.21%	102.26%, 100.30%

Table S9. Determination of TDGA with Tb-DMA in real urine samples by standard addition method.

Samples	Added (mM)	Funded (mM)	RSD (%)	Recovery (%)
		$(I_{421\text{nm}}/I_{550\text{nm}},$ $I_{452\text{nm}}/I_{550\text{nm}})$	$(I_{421\text{nm}}/I_{550\text{nm}},$ $I_{452\text{nm}}/I_{550\text{nm}})$	$(I_{421\text{nm}}/I_{550\text{nm}},$ $I_{452\text{nm}}/I_{550\text{nm}})$
Real Urine	4.98	4.61, 4.58	5.50%, 3.85%	107.96%, 108.56%
	9.90	9.11, 9.85	3.74%, 3.18%	108.70%, 100.50%
	19.61	19.48, 19.57	1.36%, 2.82%	100.66%, 100.21%

Table S10. Smartphone-based fluorescent detection of TDGA in real samples.

Samples	Materials	Spiked (mM)	Detected (mM)	RSD (%)	Recovery (%)	Smartphone Images
Real Urine	Tb-DMF	0.050	0.048	4.18%	102.75%	
		0.074	0.079	1.51%	94.45%	
		0.099	0.097	1.85%	101.95%	
Real Urine	Tb-DMA	0.099	0.093	0.54%	106.85%	
		0.123	0.114	3.24%	108.05%	
		0.148	0.153	0.91%	96.89%	

Table S11. Colour coordinates of **Ln-DMA**, **Eu_xTb_{1-x}-DMA** and **Gd_{0.95}Tb_{0.02}Eu_{0.03}-DMA** according to CIE 1931 with varied quantum yields and lifetimes.

Compounds	CIE (x, y)	Quantum yield	Lifetime
Eu-DMA	(0.675, 0.325)	13.83%	0.25 ms
Gd-DMA	(0.162, 0.194)	6.60%	49.25 ns
Tb-DMA	(0.232, 0.743)	28.21%	0.64 ms
Tb _{0.1} Eu _{0.9} -DMA	(0.644, 0.356)	20.08%	0.27 ms
Tb _{0.2} Eu _{0.8} -DMA	(0.620, 0.378)	23.41%	0.29 ms
Tb _{0.3} Eu _{0.7} -DMA	(0.548, 0.448)	13.88%	0.30 ms
Tb _{0.4} Eu _{0.6} -DMA	(0.517, 0.479)	28.85%	0.31 ms
Tb _{0.5} Tb _{0.5} -DMA	(0.439, 0.552)	17.69%	0.33 ms
Tb _{0.6} Eu _{0.4} -DMA	(0.401, 0.563)	15.68%	0.35 ms
Tb _{0.7} Eu _{0.3} -DMA	(0.353, 0.638)	17.61%	0.37 ms
Tb _{0.8} Eu _{0.2} -DMA	(0.333, 0.665)	16.03%	0.39 ms
Tb _{0.9} Eu _{0.1} -DMA	(0.262, 0.726)	13.75%	0.59 ms
Gd _{0.95} Eu _{0.03} Tb _{0.02} -DMA	(0.334, 0.353)	25.73%	—

Table S12. Summary of the quantum yields of the reported white-light-emission doped MOFs.

Compounds	Quantum yield	Ref.
La _{0.6} Eu _{0.1} Tb _{0.3} -BTPCA	47.33 %	13
1-Eu _{0.01} Gd _{0.6015} Tb _{0.3885}	36.49%	14
Y _{0.98-x} Tb _{0.02} Eu _x	28%	15
Eu _{0.0855} Gd _{0.6285} Tb _{0.2860}	22.4 %	16
Eu _{0.045} Tb _{0.955} CPOMBA	15 %	17
La _{0.6} Eu _{0.1} Tb _{0.3} CPOMBA	14.4 %	17
HMA-Tb ₁₀ Eu ₁	11.41 %	18
0.5%Eu ³⁺ -doped 2-Tb	11.4 %	19
Gd_{0.95}Eu_{0.03}Tb_{0.02}-DMA	25.73%	This work
ZJU-1:1.0%Tb ³⁺ , 2.0%Eu ³⁺ ZJU-	6.11 %	20
1:1.5%Tb ³⁺ , 2.0%Eu ³⁺	6.80 %	20

Table S13. Selected bond lengths (\AA) and angles ($^\circ$) for Eu-DMF.

Eu1–O4#1	2.406(3)	O3#1–Eu1–O5#2	135.35(9)
Eu1–O10	2.349(3)	O3#1–Eu1–O6#2	81.65(8)
Eu1–O3#1	2.406(3)	O3#1–Eu1–O12	77.74(10)
Eu1–O5#2	2.441(3)	O3#1–Eu1–O2	84.40(9)
Eu1–O6#2	2.426(2)	O5#2–Eu1–O2	89.19(10)
Eu1–O1	2.398(3)	O6#2–Eu1–O5#2	53.71(9)
Eu1–O12	2.416(3)	O6#2–Eu1–O2	82.97(9)
Eu1–O2	2.490(3)	O1–Eu1–O4#1	81.91(11)
O4#1–Eu1–O5#2	166.72(10)	O1–Eu1–O3#1	123.73(10)
O4#1–Eu1–O6#2	134.73(9)	O1–Eu1–O5#2	84.82(10)
O4#1–Eu1–O12	97.31(11)	O1–Eu1–O6#2	121.10(10)
O4#1–Eu1–O2	82.62(11)	O12–Eu1–O5#2	94.22(11)
O10–Eu1–O4#1	92.95(11)	O4–C25–Eu1#3	59.76(19)
O10–Eu1–O3#1	130.99(10)	O3–C25–Eu1#3	59.68(19)
O10–Eu1–O5#2	84.57(11)	O5–C33–Eu1#4	60.26(19)
O10–Eu1–O6#2	127.88(10)	O6–C33–Eu1#4	59.56(19)
O3#1–Eu1–O4#1	54.37(9)		

Symmetry transformations used to generate equivalent atoms: #1 1+x, -1+y, -1+z; #2 -1+x, -1+y, +z; #3 -1+x, 1+y, 1+z; #4 1+x, 1+y, +z.

Table S14. Selected bond lengths (\AA) and angles ($^\circ$) for **Gd-DMF**.

Gd1–O11	2.379(3)	O10–Gd1–O7#1	128.10(12)
Gd1–O7#1	2.398(3)	O10–Gd1–O8#2	91.93(12)
Gd1–O1	2.466(3)	O10–Gd1–O9#2	130.78(12)
Gd1–O8#2	2.387(3)	O10–Gd1–O6#1	84.57(12)
Gd1–O10	2.325(3)	O9#2–Gd1–O7#1	81.30(9)
Gd1–O9#2	2.380(3)	O9#2–Gd1–O1	84.15(10)
Gd1–O2	2.365(3)	O9#2–Gd1–O8#2	54.92(10)
Gd1–O6#1	2.415(3)	O9#2–Gd1–O6#1	135.49(10)
O1–Gd1–O4	75.69(9)	O2–Gd1–O11	148.74(11)
O11–Gd1–O7#1	80.18(11)	O2–Gd1–O7#1	121.45(11)
O11–Gd1–O8#2	97.91(12)	O2–Gd1–O8#2	82.25(12)
O11–Gd1–O9#2	78.10(11)	O2–Gd1–O9#2	124.26(11)
O11–Gd1–O6#1	93.13(12)	O2–Gd1–O6#1	84.46(11)
O7#1–Gd1–O1	82.96(10)	C22–O6–Gd1#3	93.3(2)
O7#1–Gd1–O6#1	54.20(10)	C22–O6–Gd1#3	92.7(2)
O8#2–Gd1–O7	135.14(10)	O8–C30–Gd1#4	60.1(2)
O8#2–Gd1–O1	83.28(12)	O9–C30–Gd1#4	59.7(2)
O10–Gd1–O11	71.32(12)		

Symmetry transformations used to generate equivalent atoms: #1 1+x, 1+y, +z; #2 -1+x, 1+y, 1+z; #3 -1+x, -1+y, +z; #4 1+x, -1+y, -1+z.

Table S15. Selected bond lengths (Å) and angles (°) for Eu-DMA.

Eu1–O6#1	2.433(3)	O5#1–Eu1–O11	77.67(13)
Eu1–O2#1	2.385(3)	O1–Eu1–O4#2	82.08(11)
Eu1–O5#1	2.433(3)	O10–Eu1–O6#1	84.64(14)
Eu1–O1	2.460(3)	O10–Eu1–O2	89.92(13)
Eu1–O10	2.312(4)	O10–Eu1–O5#1	131.26(13)
Eu1–O4#2	2.506(3)	O10–Eu1–O1	132.41(12)
Eu1–O11	2.446(3)	O10–Eu1–O4#2	130.60(12)
Eu1–O3#2	2.416(3)	O10–Eu1–O11	75.12(13)
O6#1–Eu1–O5#1	53.45(11)	O10–Eu1–O3#2	78.20(12)
O6#1–Eu1–O1	131.75(11)	O11–Eu1–O1	78.36(12)
O6#1–Eu1–O4#2	95.32(13)	O11–Eu1–O4#2	154.27(12)
O6#1–Eu1–O11	85.54(14)	O3#2–Eu1–O6#1	86.10(13)
O2–Eu1–O6#1	174.34(13)	O3#2–Eu1–O5#1	117.02(12)
O2–Eu1–O5#1	132.10(11)	O3#2–Eu1–O1	125.49(11)
O2–Eu1–O1	53.63(11)	O3#2–Eu1–O42	52.62(11)
O2–Eu1–O4#2	87.03(13)	O3#2–Eu1–O11	152.66(13)
O2–Eu1–O11	94.57(15)	O4–C22–Eu1#4	62.2(2)
O2–Eu1–O3#2	91.28(13)	O3–C22–Eu1#4	58.1(2)
O5#1–Eu1–O1	78.63(10)	O5–C30–Eu1#3	59.8(2)
O5#1–Eu1–O4#2	82.25(11)	O6–C30–Eu1#3	59.8(2)

Symmetry transformations used to generate equivalent atoms: #1 -2+x, +y, 1+z; #2 -1+x, 1+y, 1+z; #3 2+x, +y, 1+z; #4 1+x, -1+y, -1+z.

Table S16. Selected bond lengths (\AA) and angles ($^{\circ}$) for **Gd-DMA**.

Gd1–O2	2.377(4)	O10–Gd1–O5#1	78.21(14)
Gd1–O5#1	2.414(4)	O10–Gd1–O3#2	84.50(15)
Gd1–O10	2.310(4)	O10–Gd1–O1	132.35(14)
Gd1–O3#2	2.431(4)	O10–Gd1–O4#2	131.10(14)
Gd1–O1	2.444(4)	O10–Gd1–O11	75.19(15)
Gd1–O4#2	2.422(4)	O10–Gd1–O6#1	130.70(13)
Gd1–O11	2.433(4)	O3#2–Gd1–O1	132.09(12)
Gd1–O6#1	2.502(4)	O3#2–Gd1–O11	86.33(17)
O2–Gd1–O5#1	91.11(15)	O3#2–Gd1–O6#1	95.24(15)
O2–Gd1–O3#2	173.76(13)	O1–Gd1–O6#1	82.00(13)
O2–Gd1–O1	53.88(12)	O4#2–Gd1–O3#2	53.67(12)
O2–Gd1–O4#2	132.46(13)	O4#2–Gd1–O1	78.71(12)
O2–Gd1–O11	93.86(18)	O4#2–Gd1–O11	77.75(16)
O2–Gd1–O6#1	87.32(15)	O4#2–Gd1–O6#1	82.41(13)
O5#1–Gd1–O3#2	85.95(14)	O11–Gd1–O1	77.95(15)
O5#1–Gd1–O1	125.37(13)	O11–Gd1–O6#1	154.11(14)
O5#1–Gd1–O4#2	117.31(14)	O5–C22–Gd1#3	57.9(3)
O5#1–Gd1–O11	152.88(15)	O6–C22–Gd1#3	62.0(3)
O5#1–Gd1–O6#1	52.71(13)	O3–C30–Gd1#4	60.7(3)
O10–Gd1–O2	89.51(15)	O4–C30–Gd1#4	60.3(3)

Symmetry transformations used to generate equivalent atoms: #1 $-1+x, 1+y, 1+z$; #2 $-2+x, +y, 1+z$; #3 $1+x, -1+y, -1+z$; #4 $2+x, +y, -1+z$.

Reference

1. X. K. Song, Y. Zou, X. F. Liu, M. Oh and M. S. Lah, A two-fold interpenetrated (3,6)-connected metal–organic framework with rutile topology showing a large solvent cavity, *New. J. Chem.*, 2010, **34**, 2396–2399.
2. M. J. Frisch, G. W. Trucks, H. B. Schlegel, G. E. Scuseria, M. A. Robb, J. R. Cheeseman, G. Scalmani, V. Barone, B. Mennucci, G. A. Petersson, H. Nakatsuji, M. Caricato, X. Li, H. P. Hratchian, A. F. Izmaylov, J. Bloino, G. Zheng, J. L. Sonnenberg, M. Hada, M. Ehara, K. Toyota, R. Fukuda, J. Hasegawa, M. Ishida, T. Nakajima, Y. Honda, O. Kitao, H. Nakai, T. Vreven, J. A. Jr. Montgomery, J. E. Peralta, F. Ogliaro, M. Bearpark, J. J. Heyd, E. Brothers, K. N. Kudin, V. N. Staroverov, R. Kobayashi, J. Normand, K. Raghavachari, A. Rendell, J. C. Burant, S. S. Iyengar, J. Tomasi, M. Cossi, N. Rega, J. M. Millam, M. Klene, J. E. Knox, J. B. Cross, V. Bakken, C. Adamo, J. Jaramillo, R. Gomperts, R. E. Stratmann, O. Yazyev, A. J. Austin, R. Cammi, C. Pomelli, J. W. Ochterski, R. L. Martin, K. Morokuma, V. G. Zakrzewski, G. A. Voth, P. Salvador, J. J. Dannenberg, S. Dapprich, A. D. Daniels, O. Farkas, J. B. Foresman, J. V. Ortiz, J. Cioslowski and D. J. Fox, Gaussian 09, Revision A. 02.
3. T. Lu and F. Chen, Multiwfn: A multifunctional wavefunction analyzer, *J. Comput. Chem.*, 2012, **33**, 580–592.
4. W. Humphrey, A. Dalke and K. Schulten, VMD: Visual molecular dynamics, *J. Mol. Graph.*, 1996, **14**, 33–38.
5. O. V. Dolomanov, L. J. Bourhis, R. J. Gildea, J. A. K. Howard and H. Puschmann, OLEX2: a complete structure solution, refinement and analysis program, *J. Appl. Cryst.*, 2009, **42**, 339–341.
6. Z. X. Zhu, C. J. Wang, D. Luo, C. Liu, D. N. Liu, Y. M. Xiao, S. Chen and Y. Y. Wang, Six new lanthanide metal–organic frameworks as luminescent sensors for the detection of 1-N, TDGA, UA, and HA in urine, *J. Coord. Chem.*, 2019, **72**, 3526–3543.
7. J. N. Hao, X. Y. Xu, X. Lian, C. Zhang and B. Yan, A Luminescent 3d-4f-4d MOF Nanoprobe as a Diagnosis Platform for Human Occupational Exposure to Vinyl Chloride Carcinogen, *Inorg. Chem.*, 2017, **56**, 11176–11183.
8. Y. C. Fan, X. Jiang, J. Che, M. F. Li, X. J. Zhang, D. J. Gao, J. Bi and Z. L. Ning, A Ratiometric Fluorescent Sensor Based on Dye/Tb (III) Functionalized UiO-66 for Highly Sensitive Detection of TDGA, *Molecules.*, 2022, **27**, 6543.

9. N. Wu, H. Guo, L. P. Peng, M. Y. Wang, Y. J. Cao, M. Yang, L. Sun and W. Yang, A novel core-shell nanomaterial ratiometric fluorescent probe for detecting urinary TDGA as a biomarker for VCM exposure, *Sensor Actuat B-chem.*, 2021, **345**, 130402.
10. Y. S. Liu, M. Y. Wang, Y. F. Hui, J. Y. Tian, J. X. Xu, Z. Y. Lu, Z. Y. Yang, H. Guo and W. Yang, Eu³⁺-Modified Covalent Organic Frameworks for the Detection of a Vinyl Chloride Monomer Exposure Biomarker, *ACS Sensors.*, 2023, **9**, 315–324.
11. T. Baygildiev, A. Braun, A. Stavrianidi, I. Rodin, O. Shpigun, I. Rybalchenko and I. Ananieva, Dilute-and-shoot” rapid-separation liquid chromatography tandem mass spectrometry method for fast detection of thiodiglycolic acid in urine, *Eur. Mass Spectrom.*, 2015, **21**, 733–738.
12. Z. Dlaskova, T. Navratil, M. Heyrovsky, D. Pelclova and L. Novotny, Voltammetric determination of thiodiglycolic acid in urine, *Anal. Bioanal. Chem.*, 2003, **375**, 164–168.
13. Q. Tang, S. X. Liu, Y. W. Liu, D. F. He, J. Miao, X. Q. Wang, Y. J. Ji and Z. P. Zheng, Color Tuning and White Light Emission via in Situ Doping of Luminescent Lanthanide Metal–Organic Frameworks, *Inorg. Chem.*, 2014, **53**, 289–293.
14. L. L. Ma, G. P. Yang, G. P. Li, P. F. Zhang, J. Jin, Y. Wang, J. M. Wang and Y. Y. Wang, Luminescence modulation, near white light emission, selective luminescence sensing, and anticounterfeiting via a series of Ln-MOFs with a π-conjugated and uncoordinated lewis basic triazolyl ligand, *Inorg. Chem. Front.*, 2021, **8**, 329–338.
15. K. Manna, J. P. Sutter and S. Natarajan, Blue-Emitting Ligand-Mediated Assembly of Rare-Earth MOFs toward White-Light Emission, Sensing, Magnetic, and Catalytic Studies, *Inorg. Chem.*, 2022, **61**, 16770–16785.
16. X. Y. Li, W. J. Shi, X. Q. Wang, L. N. Ma, L. Hou and Y. Y. Wang, Luminescence Modulation, White Light Emission, and Energy Transfer in a Family of Lanthanide Metal–Organic Frameworks Based on a Planar π-Conjugated Ligand, *Cryst. Growth Des.*, 2017, **17**, 4217–4224.
17. Y. W. Zhao, F. Q. Zhang and X. M. Zhang, Single Component Lanthanide Hybrids Based on Metal–Organic Framework for Near–Ultraviolet White Light LED, *ACS Appl. Mater. Interfaces.*, 2016, **8**, 24123–24130.

18. H. P. Liu, T. S. Chu, Z. L. Rao, S. Y. Wang, Y. Y. Yang and W. T. Wong, The Tunable White–Light and Multicolor Emission in an Electrodeposited Thin Film of Mixed Lanthanide Coordination Polymers, *Adv. Opt. Mater.*, 2015, **3**, 1545–1550.
19. Z. F. Liu, M. F. Wu, S. H. Wang, F. K. Zheng, G. E. Wang, J. Chen, Y. Xiao, A. Q. Wu, G. C. Guo and J. S. Huang, J. S. Eu³⁺–Doped Tb³⁺ Metal–Organic Frameworks Emitting Tunable Three Primary Colors Towards White Light, *J. Mater. Chem. C.*, 2013, **1**, 4634–4639.
20. X. T. Rao, Q. Huang, X. L. Yang, Y. J. Cui, Y. Yang, C. D. Wu, B. L. Chen and G. D. Qian, Color tunable and white light emitting Tb³⁺ and Eu³⁺ doped lanthanide metal–organic framework materials, *J. Mater. Chem.*, 2012, **22**, 3210–3214.